Neuron

Article

Selective removal of astrocytic PERK protects against glymphatic impairment and decreases toxic aggregation of β-amyloid and tau

Highlights

- Astrocyte-specific PERK deletion restores protein synthesis and glymphatic function
- Removal of astrocytic PERK reduces Aβ and tau aggregation
- Cognitive performance is improved after astrocytic PERK deletion
- Chronic PERK signaling disrupts perivascular AQP4 localization via CK2

Authors

Kai Chen, Yosuke M. Morizawa, Tal Nuriel, Osama Al-Dalahmah, Zhongcong Xie, Guang Yang

Correspondence

zhongcong.Xie@uth.tmc.edu (Z.X.), gy2268@cumc.columbia.edu (G.Y.)

In brief

Chen et al. show that in AD mouse models, chronic activation of astrocytic PERK-eIF2a signaling suppresses protein synthesis and disrupts perivascular AQP4 localization via CK2-dependent mechanisms. Inhibiting astrocytic PERK restores glymphatic function, reduces AD-related pathology, and improves cognitive performance.

Chen et al., 2025, Neuron *113*, 1–17
August 6, 2025
https://doi.org/10.1016/j.neuron.2025.04.027

CellPress

Neuron

CellPress

Article

Selective removal of astrocytic PERK protects against glymphatic impairment and decreases toxic aggregation of β-amyloid and tau

Kai Chen,[1] Yosuke M. Morizawa,[1] Tal Nuriel,[2,3] Osama Al-Dalahmah,[2,3] Zhongcong Xie,[4,5,*] and Guang Yang[1,6,*]
[1]Department of Anesthesiology, Columbia University Irving Medical Center, New York, NY 10032, USA
[2]Taub Institute for Research on Alzheimer's Disease and the Aging Brain, Columbia University Irving Medical Center, New York, NY 10032, USA
[3]Department of Pathology and Cell Biology, Columbia University Irving Medical Center, New York, NY 10032, USA
[4]Geriatric Anesthesia Research Unit, Department of Anesthesia, Critical Care and Pain Medicine, Massachusetts General Hospital and Harvard Medical School, Charlestown, MA 02129, USA
[5]Present address: Department of Anesthesiology, Critical Care and Pain Medicine, McGovern Medical School, The University of Texas Health Science Center at Houston, Houston, TX 77030, USA
[6]Lead contact
*Correspondence: zhongcong.Xie@uth.tmc.edu (Z.X.), gy2268@cumc.columbia.edu (G.Y.)
https://doi.org/10.1016/j.neuron.2025.04.027

SUMMARY

Dysfunction of the glymphatic system, a brain-wide waste clearance network, is strongly linked to Alzheimer's disease (AD) and the accumulation of β-amyloid (Aβ) and tau proteins. Here, we identify an astrocytic signaling pathway that can be targeted to preserve glymphatic function and mitigate neurotoxic protein buildup. Analysis of astrocytes from both human AD brains and two transgenic mouse models (5XFAD and PS19) reveals robust activation of the protein kinase RNA-like endoplasmic reticulum (ER) kinase (PERK)-α subunit of eukaryotic initiation factor 2 (eIF2α) branch of the unfolded protein response. Chronic PERK activation suppresses astrocytic protein synthesis and, through casein kinase 2 (CK2)-dependent mechanisms, disrupts the perivascular localization of aquaporin-4 (AQP4), a water channel essential for glymphatic flow. Importantly, astrocyte-specific PERK deletion or pharmacological inhibition restores AQP4 localization, enhances glymphatic clearance, reduces Aβ and tau pathology, and improves cognitive performance in mice. These findings highlight the critical role of the astrocytic PERK-CK2-AQP4 axis in glymphatic dysfunction and AD pathogenesis, positioning this pathway as a promising therapeutic target.

INTRODUCTION

Alzheimer's disease (AD), a leading cause of dementia worldwide, is characterized by the progressive accumulation of aggregated β-amyloid (Aβ) and hyperphosphorylated tau proteins in the brain.[1,2] This pathological protein buildup, along with metabolic disturbances and oxidative stress, disrupts cellular homeostasis and contributes to neurodegeneration and cognitive impairment. The unfolded protein response (UPR) is a critical mechanism for maintaining cellular homeostasis during endoplasmic reticulum (ER) stress.[3] Among the three major branches of the UPR, the protein kinase RNA-like ER kinase (PERK) pathway plays a central role in regulating protein synthesis as part of the adaptive response.[4] Under normal conditions, PERK remains inactive through its association with the ER chaperone binding immunoglobulin protein (BiP). Upon ER stress, triggered by the accumulation of misfolded or unfolded proteins, BiP dissociates from PERK, allowing its activation. Activated PERK phosphorylates the α subunit of eukaryotic initiation factor 2 (eIF2α), leading to a temporary reduction in global protein translation. While transient ER stress can be resolved through adaptive UPR signaling, chronic or excessive ER stress leads to sustained UPR activation. In several neurodegenerative mouse models, chronic activation of the PERK-eIF2α pathway results in persistent suppression of protein synthesis, ultimately causing synaptic dysfunction and neuronal loss.[5–7]

Although neuronal UPR activation has been extensively documented in neurodegenerative diseases,[8,9] including AD, the contribution of astrocytic UPR signaling to disease progression remains less well understood.[10] Astrocytes play essential roles in regulating the brain's glymphatic system, a perivascular fluid transport network formed by astroglial endfeet that envelop the cerebral vasculature.[11,12] This system facilitates the exchange of cerebrospinal fluid (CSF) and interstitial fluid (ISF), supporting the clearance of metabolic waste and neurotoxic proteins such as Aβ and tau.[12–15] These solutes are eventually drained through cervical lymphatic pathways, including meningeal lymphatic

Please cite this article in press as: Chen et al., Selective removal of astrocytic PERK protects against glymphatic impairment and decreases toxic aggregation of β-amyloid and tau, Neuron (2025), https://doi.org/10.1016/j.neuron.2025.04.027

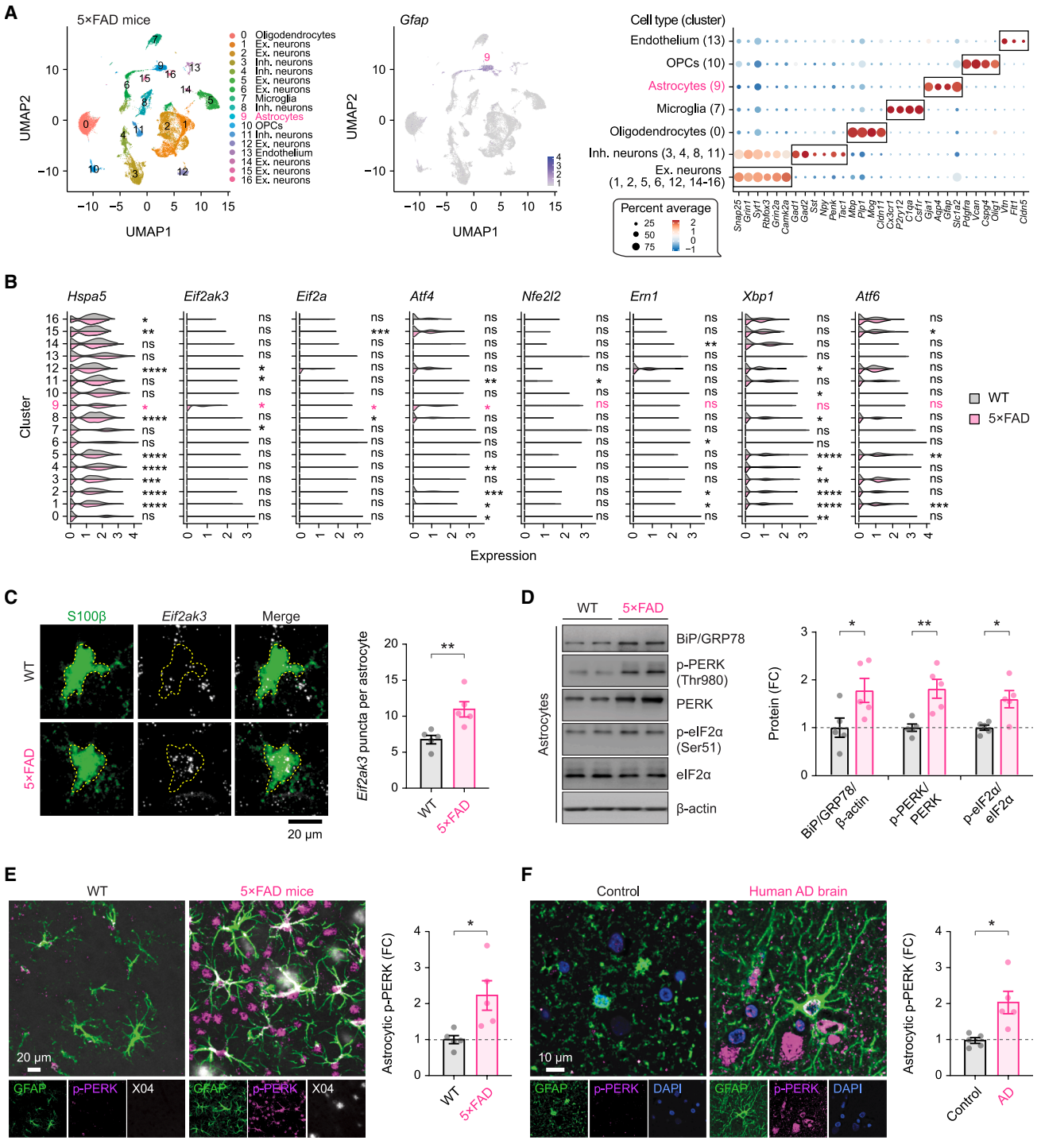

Figure 1. Astrocytic PERK-eIF2α signaling is strongly activated in human AD brains and mouse models

(A) snRNA-seq analysis of the cerebral cortex from 7-month-old WT and 5XFAD mice (n = 3 mice per group). The UMAP plot (left) shows 17 distinct cell clusters (0–16) with cell-type identities determined using established marker genes (right). Cluster 9 corresponds to astrocytes.

(B) Expression levels of key UPR genes across clusters identified in (A).

(C) Left, RNAscope *in situ* hybridization of *Eif2ak3* in the cortex of 6-month-old WT and 5XFAD mice (n = 5 mice per group). Right, quantification of *Eif2ak3* puncta in S100β$^+$ astrocytes (p = 0.0083).

(D) Left, western blot analysis of cortical astrocytes isolated from 6-month-old WT and 5XFAD mice (n = 5 mice per group), probed with the indicated antibodies. Right, densitometric quantification (p = 0.0418, p = 0.0049, and p = 0.0130).

(legend continued on next page)

Please cite this article in press as: Chen et al., Selective removal of astrocytic PERK protects against glymphatic impairment and decreases toxic aggregation of β-amyloid and tau, Neuron (2025), https://doi.org/10.1016/j.neuron.2025.04.027

vessels.[16–19] Rodent studies have shown that glymphatic exchange depends on aquaporin-4 (AQP4),[12,13,20] a water channel highly enriched at perivascular astrocytic endfeet.[21] Disruption of AQP4 expression or its polarized perivascular localization exacerbates Aβ plaque deposition and tau aggregation in AD mouse models,[13,22,23] as well as in models involving AD-related risk factors.[24,25] Consistently, in human AD brain tissue, reduced perivascular AQP4 localization correlates with greater Aβ and tau pathology and worse cognitive performance.[26,27] Given the critical roles of astrocytes in glymphatic clearance and the involvement of UPR signaling in AD pathogenesis, we investigated whether astrocytic UPR contributes to glymphatic dysfunction and the progression of AD pathology.

RESULTS

Astrocytic PERK-eIF2α signaling is strongly activated in AD transgenic mice and human AD brains

To examine astrocytic UPR signaling in AD, we analyzed a single-nucleus RNA sequencing (snRNA-seq) dataset (GEO: GSE140511) derived from the cerebral cortex of 7-month-old 5XFAD transgenic AD mice and wild-type (WT) controls.[28] The UPR comprises three major branches: the PERK-eIF2α, inositol-requiring enzyme 1α (IRE1α)-X-box binding protein 1 (XBP1), and activating transcription factor 6 (ATF6) pathways.[3,4] Within the astrocyte cluster, we observed significant upregulation of genes associated with the PERK-eIF2α pathway, including *Hspa5* (encoding BiP), *Eif2ak3* (PERK), *Eif2a*, and *Atf4*, in 5XFAD mice relative to WT controls (Figures 1A, 1B, and S1). By contrast, expression of genes involved in the IRE1α-XBP1 and ATF6 pathways (e.g., *Ern1*, *Xbp1*, and *Atf6*) did not differ significantly between genotypes (Figure 1B). Fluorescence *in situ* hybridization further confirmed increased *Eif2ak3* mRNA expression in cortical astrocytes of 6-month-old 5XFAD mice ($p = 0.0083$; Figure 1C).

To validate PERK-eIF2α pathway activation at the protein level, we performed western blot analysis on astrocytes isolated from the cortex of 6-month-old 5XFAD and WT mice. Consistent with transcriptomic findings, 5XFAD astrocytes exhibited elevated BiP expression and increased phosphorylation of both PERK and eIF2α compared with WT controls (Figure 1D). Immunofluorescence staining revealed a 2.2-fold increase in phosphorylated PERK levels in astrocytes of 5XFAD mice ($p = 0.02$; Figure 1E). Similarly, post-mortem brain tissue from individuals with AD showed significantly elevated phosphorylated PERK in astrocytes compared with non-AD controls ($p = 0.01$; Figure 1F; Table S1). Together, these results from both mouse models and human samples demonstrate robust activation of the astrocytic PERK-eIF2α signaling pathway in AD.

Astrocytic PERK deletion enhances perivascular AQP4 localization and glymphatic function

To investigate the role of astrocytic PERK signaling in AD pathology, we generated 5XFAD mice with astrocyte-specific PERK deletion by crossing 5XFAD mice with PERK$^{fl/fl}$;Aldh1l1$^{CreER/+}$ mice (Figures 2A and S2A). This inducible model expresses tamoxifen-activated CreER recombinase under the astrocyte-specific *Aldh1l1* promoter[29] and harbors a floxed *Perk* allele.[30] At 2 months of age, mice received 4-hydroxytamoxifen (4-OHT; 50 mg/kg) for 3 consecutive days to induce CreER-mediated PERK deletion. Astrocyte-specific PERK deletion was confirmed by immunoblotting (Figure S2B) and immunofluorescence staining (Figure S2C).

Given PERK's role in eIF2α-dependent translational control,[4,31] we assessed *de novo* protein synthesis in cortical astrocytes at 6 months of age using surface sensing of translation (SUnSET) labeling with puromycin in awake mice (see STAR Methods).[32] Compared with WT controls, 5XFAD mice exhibited a marked reduction in astrocytic protein synthesis, with puromycin staining inversely correlated with phosphorylated PERK levels (Figures S2D–S2F). Western blot analysis of isolated astrocytes confirmed reduced protein synthesis in 5XFAD mice (5XFAD;PERK$^{fl/fl}$) relative to WT controls (PERK$^{fl/fl}$), and astrocytic PERK deletion partially restored protein synthesis in 5XFAD mice (Figure 2B).

The astrocytic water channel AQP4, essential for glymphatic exchange, exhibits impaired perivascular localization in AD.[26,27] To assess whether PERK signaling contributes to AQP4 mislocalization, we examined AQP4 expression and localization in the cortex of 5XFAD mice with or without astrocytic PERK deletion. Although total AQP4 protein levels were unchanged (Figures S3A and S3B), immunofluorescence analysis revealed significantly reduced perivascular AQP4 localization in 5XFAD mice compared with WT controls (Figures 2C and S3C; see STAR Methods), which was partially restored by astrocytic PERK deletion. These findings were corroborated by western blot analysis of AQP4 levels in isolated cortical vessels (Figure 2D; see STAR Methods). PERK deletion in WT mice had no effect on AQP4 expression or localization (Figures 2C, 2D, and S3A–S3C).

To evaluate glymphatic function, we performed *in vivo* two-photon imaging to monitor the influx of a fluorescent CSF tracer, fluorescein isothiocyanate-dextran (FITC-dextran; 3 kDa), delivered into the cisterna magna (Figure 2E). Cerebral vasculature was visualized via retro-orbital injection of Texas red. In WT mice, tracer penetrated the brain parenchyma along periarteriolar spaces within 10 min, reaching peak distribution by 50 min (Figure 2F). By contrast, 5XFAD mice showed delayed tracer influx, requiring ~50 min to reach comparable depths, consistent with impaired glymphatic function. Astrocytic PERK deletion

(E) Left, representative images of cortical sections stained for GFAP (astrocytes), phosphorylated PERK (p-PERK), and amyloid plaques (methoxy-X04) in 6-month-old WT and 5XFAD mice ($n = 5$ mice per group). Right, quantification of p-PERK fluorescence intensity in GFAP$^+$ astrocytes ($p = 0.0201$).
(F) Left, representative images of post-mortem human anterior cingulate cortex stained for GFAP, p-PERK, and DAPI from control and AD individuals ($n = 5$ samples per group). Right, quantification of p-PERK fluorescence intensity in GFAP$^+$ astrocytes ($p = 0.0112$).
Data are presented as mean ± SEM. ns, not significant; $^*p < 0.05$, $^{**}p < 0.01$, $^{***}p < 0.001$, $^{****}p < 0.0001$; by Wilcoxon rank-sum test (B) or two-tailed unpaired t test (C–F). FC, fold change.
See also Figure S1 and Table S1.

Please cite this article in press as: Chen et al., Selective removal of astrocytic PERK protects against glymphatic impairment and decreases toxic aggregation of β-amyloid and tau, Neuron (2025), https://doi.org/10.1016/j.neuron.2025.04.027

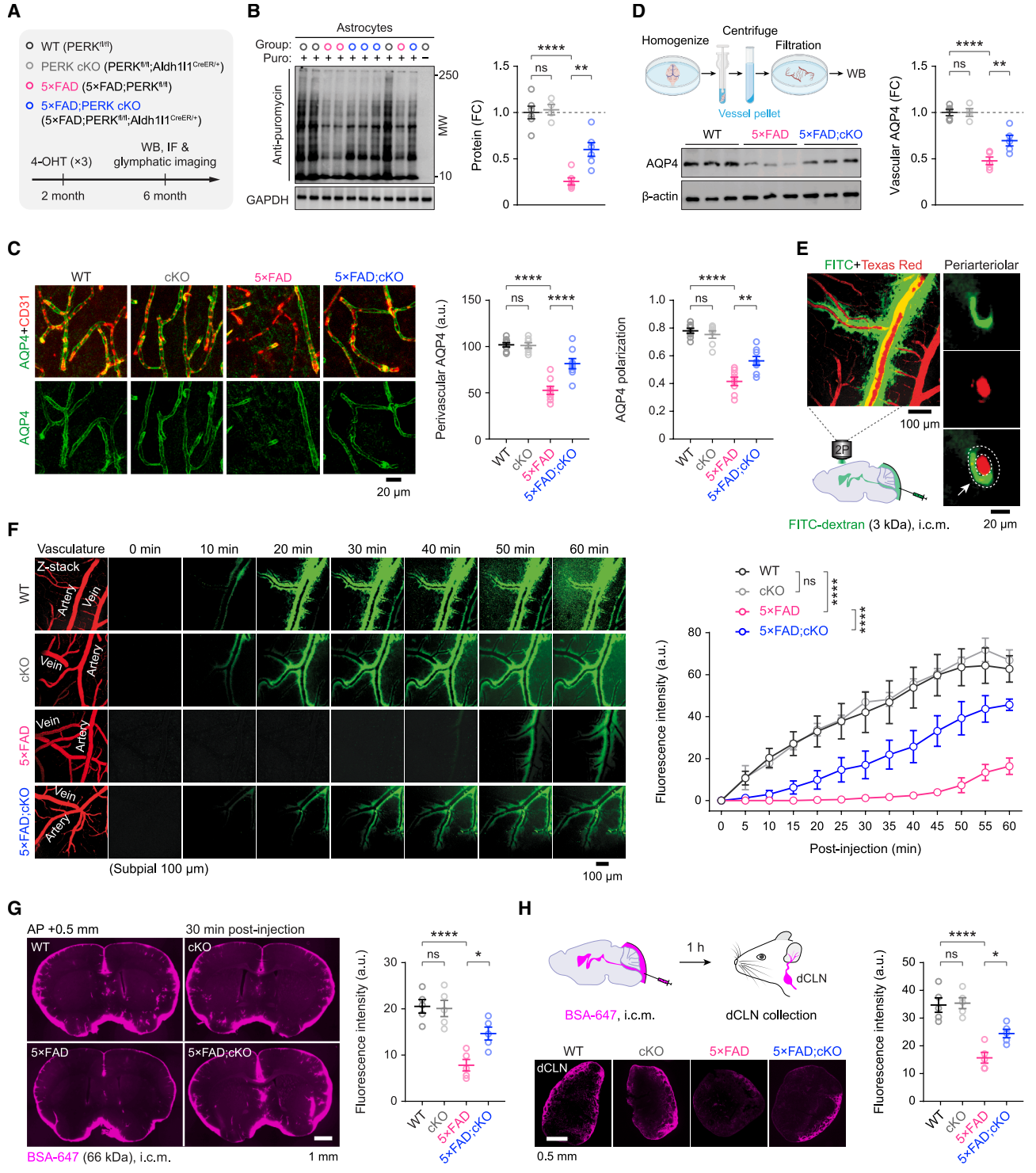

Figure 2. Astrocytic PERK deletion enhances perivascular AQP4 localization and improves glymphatic function in 5XFAD mice

(A) Experimental timeline for astrocyte-specific PERK conditional knockout (cKO) and subsequent analyses.

(B) Western blot analysis of puromycin-labeled proteins in isolated cortical astrocytes (n = 6, 4, 6, 6 mice; $p > 0.9999$, $p < 0.0001$, $p = 0.0022$).

(C) Left, representative images of cortical sections immunostained for AQP4 and the vascular marker CD31 (n = 8, 7, 8, 8 mice). Right, quantification of perivascular AQP4 expression ($p > 0.9999$, $p < 0.0001$, $p < 0.0001$) and AQP4 polarization ($p > 0.9999$, $p < 0.0001$, $p = 0.0015$).

(D) Western blot analysis of AQP4 protein levels in isolated cerebral vessels (n = 5, 4, 5, 5 mice; $p > 0.9999$, $p < 0.0001$, $p = 0.0093$). Illustration created with Biorender.com.

(legend continued on next page)

partially rescued CSF tracer influx in 5XFAD mice. These findings were validated using *ex vivo* imaging following intracisternal injection of Alexa Fluor 647-conjugated bovine serum albumin (BSA-647; 66 kDa) (Figure 2G).

To assess CSF efflux to the deep cervical lymph nodes (dCLNs), BSA-647 was injected into the cisterna magna, and tracer accumulation in dCLNs was measured 1 h later (Figure 2H). WT mice showed robust tracer accumulation, while 5XFAD mice exhibited reduced levels, indicative of impaired CSF drainage. Astrocytic PERK deletion significantly improved tracer clearance to the dCLNs in 5XFAD mice without altering the morphology or coverage of meningeal lymphatic vessels (Figure S3D).

Collectively, these results demonstrate that astrocytic PERK deletion restores protein synthesis, improves perivascular AQP4 localization, and enhances glymphatic function in 5XFAD mice.

Astrocytic PERK deletion alleviates Aβ deposition, neuroinflammation, and cognitive decline

AQP4 deficiency and impaired glymphatic function have been implicated in promoting Aβ plaque accumulation in AD models.[22,23] Given that astrocytic PERK deletion enhances perivascular AQP4 localization and glymphatic function (Figure 2), we next examined its impact on Aβ pathology. In 5XFAD mice, amyloid deposition begins around 2 months of age, with substantial Aβ accumulation, glial activation, and cognitive deficits evident by 6 months[33] (Figure 3A). As expected, extensive Aβ deposition was observed in the cortex and hippocampus of 6-month-old 5XFAD mice. By contrast, 5XFAD mice with astrocytic PERK deletion exhibited significantly lower levels of both soluble and insoluble $A\beta_{42}$ in cortical (Figure 3B) and hippocampal (Figure 3C) lysates, as measured by ELISA. Immunohistochemical analysis further confirmed reduced total Aβ (D54D2 staining; Figure 3D) and plaque burden (6E10 staining; Figure 3E) in PERK-deleted 5XFAD mice. Notably, administration of the selective AQP4 inhibitor TGN-020 abolished the Aβ-lowering effect of astrocytic PERK deletion (Figures S4A–S4E), indicating that this effect is AQP4-dependent.

At 6 months of age, 5XFAD mice also exhibited pronounced glial activation in the cortical parenchyma. Astrocytic PERK deletion significantly reduced GFAP and Iba-1 immunoreactivity (Figures S4F and S4G), suggesting attenuation of both astrocytic and microglial activation. Correspondingly, levels of proinflammatory cytokines interleukin-1β (IL-1β) and tumor necrosis factor alpha (TNF-α) were significantly decreased in PERK-deleted 5XFAD mice compared with PERK-intact controls (Figure S4H).

In brain border regions, 5XFAD mice showed altered parenchymal border macrophage (PBM) subtypes, with an increase in $MHCII^+CD206^+$ PBMs (associated with immune response) and a decrease in $LYVE1^+CD206^+$ PBMs (which regulate CSF flow dynamics[34,35]) relative to WT controls. These PBM alterations were partially reversed by astrocytic PERK deletion (Figure S4I).

To assess cognitive performance, we evaluated 5XFAD mice following astrocytic PERK deletion using the Barnes maze (Figure 3F), a test of spatial learning and memory.[36] During the training phase (days 1–4), 5XFAD mice exhibited significantly longer escape latencies compared with WT controls (Figure 3G). In the probe trial (day 5), PERK-deleted 5XFAD mice spent significantly more time in the target quadrant than PERK-intact 5XFAD mice, indicating improved spatial memory. Astrocytic PERK deletion also enhanced associative fear memory, as evidenced by increased freezing responses in the auditory-cued fear conditioning test both 1 and 7 days after training, compared with PERK-intact 5XFAD controls (Figures 3H and 3I).

Together, these results demonstrate that astrocytic PERK deletion reduces amyloid pathology, attenuates neuroinflammation, and rescues cognitive deficits in 5XFAD mice.

Inhibiting PERK phosphorylation improves glymphatic function and mitigates AD pathology

Having established a key role for astrocytic PERK signaling in glymphatic dysfunction and amyloid pathology, we next investigated whether pharmacological inhibition of PERK could provide therapeutic benefits in 5XFAD mice. 4-month-old 5XFAD mice were chronically treated with the selective PERK inhibitor GSK2606414 (GSK; 1 mM, 0.15 μL/h, intracisterna magna [i.c.m.]) or vehicle via osmotic minipumps (Figure 4A; see STAR Methods). After 6 weeks of treatment, GSK-treated 5XFAD mice showed a significant increase in *de novo* protein synthesis in cortical astrocytes (Figure 4B), confirming effective suppression of PERK-eIF2α signaling. This restoration of protein synthesis was accompanied by improved perivascular AQP4 localization (Figure 4C) and enhanced glymphatic function, as indicated by increased CSF tracer penetration into the brain parenchyma relative to vehicle-treated controls (Figure 4D).

Consistent with improved glymphatic function, GSK-treated mice exhibited significantly reduced Aβ deposition in both the cortex and hippocampus (Figure 4E). Behavioral assessment

(E) *In vivo* two-photon imaging of the mouse cortex showing Texas red-labeled vasculature and FITC-dextran tracer distribution along periarteriolar spaces. Dashed lines indicate periarteriolar spaces.
(F) Left, representative time-lapse images showing FITC-dextran tracer distribution in the cortex following intracisternal injection (n = 6, 4, 6, 7 mice). Right, quantification of average fluorescence intensity in periarteriolar spaces ($p > 0.9999$, $p < 0.0001$, $p < 0.0001$).
(G) Left, representative coronal brain sections (0.5 mm from bregma) showing BSA-647 tracer distribution 30 min after intracisternal injection (n = 5 mice per group). Right, quantification of fluorescence intensity in the somatosensory cortex across three coronal sections spanning −1.0 to +1.0 mm from bregma ($p > 0.9999$, $p < 0.0001$, $p = 0.0138$).
(H) Assessment of CSF tracer efflux to the deep cervical lymph nodes (dCLNs). Left, dCLNs collected 1 h after intracisternal injection of BSA-647 (n = 5 mice per group). Right, quantification of tracer fluorescence intensity in dCLNs ($p > 0.9999$, $p < 0.0001$, $p = 0.0234$).
Data are presented as mean ± SEM. ns, not significant; $^*p < 0.05$, $^{**}p < 0.01$, $^{****}p < 0.0001$; by one-way ANOVA (B–D, G, and H) or two-way ANOVA (F) followed by Bonferroni's test. FC, fold change; a.u., arbitrary units.
See also Figures S2 and S3.

Please cite this article in press as: Chen et al., Selective removal of astrocytic PERK protects against glymphatic impairment and decreases toxic aggregation of β-amyloid and tau, Neuron (2025), https://doi.org/10.1016/j.neuron.2025.04.027

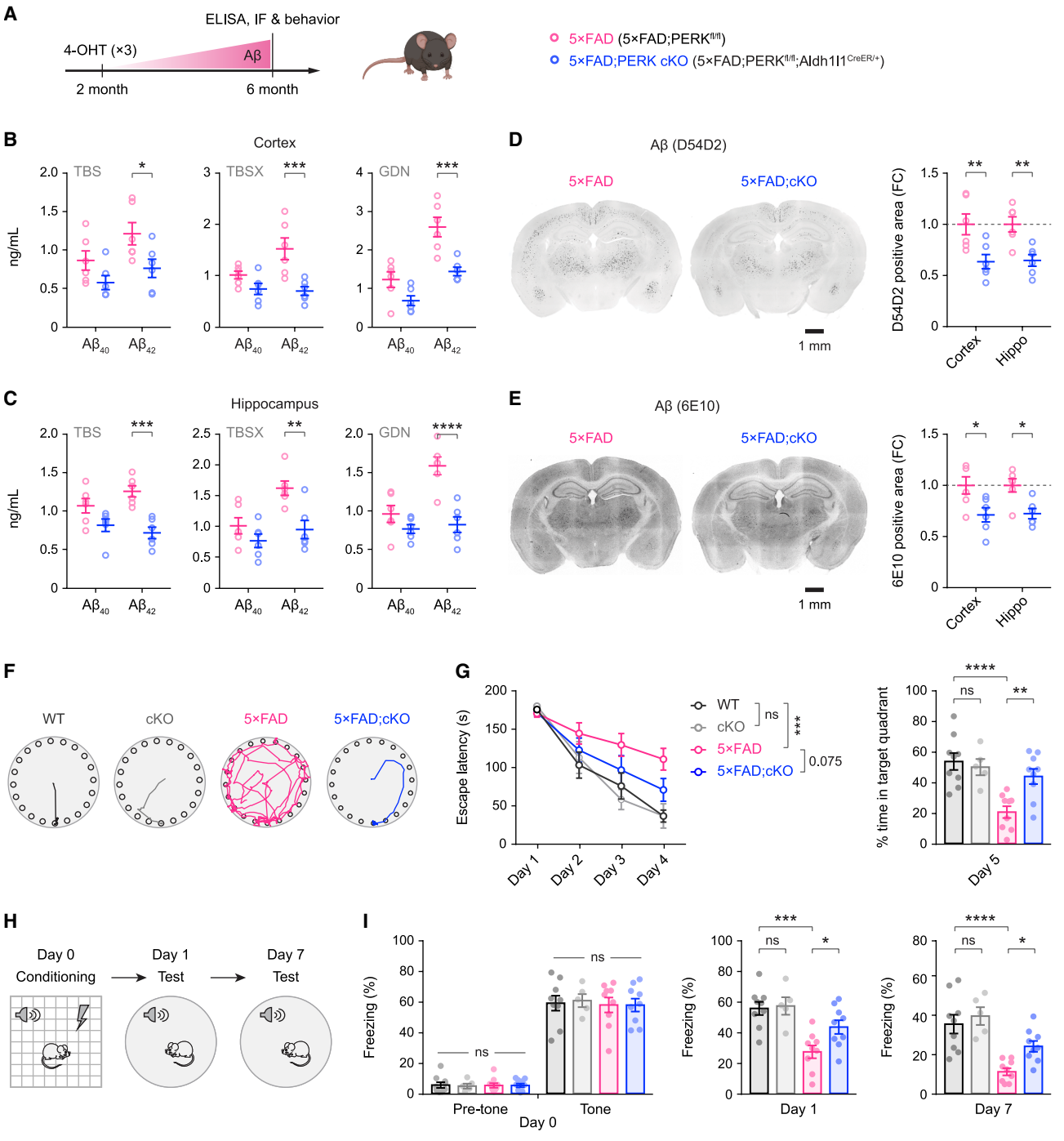

Figure 3. Deletion of astrocytic PERK reduces Aβ deposition and improves memory in 5XFAD mice

(A) Experimental timeline.

(B) ELISA quantification of $A\beta_{40}$ and $A\beta_{42}$ levels in cortical lysates ($n = 6$ mice per group), sequentially extracted with tris-buffered saline (TBS; soluble fraction: $p = 0.2197$, $p = 0.0333$), TBS + 1% Triton X-100 (TBSX; detergent-soluble fraction: $p = 0.3228$, $p = 0.0005$), and guanidine hydrochloride (GDN; detergent-insoluble fraction: $p = 0.0943$, $p = 0.0005$).

(C) ELISA quantification of $A\beta_{40}$ and $A\beta_{42}$ in hippocampal lysates ($n = 6$ mice per group), measured in TBS ($p = 0.0777$, $p = 0.0003$), TBSX ($p = 0.3804$, $p = 0.0026$), and GDN ($p = 0.3539$, $p < 0.0001$) fractions.

(D) Left, representative brain sections stained with anti-Aβ antibody (D5452) ($n = 6$ mice per group). Right, quantification of Aβ burden in the cortex ($p = 0.0065$) and hippocampus ($p = 0.0083$).

(legend continued on next page)

further revealed enhanced cognitive performance, as indicated by increased freezing responses in the auditory-cued fear conditioning test relative to vehicle-treated controls (Figure 4F). These findings are consistent with previous reports demonstrating the neuroprotective and cognitive benefits of PERK inhibition in models of neurodegeneration[6,10,37] and collectively support the therapeutic potential of targeting PERK signaling to enhance glymphatic function, reduce amyloid pathology, and improve cognitive outcomes in AD.

Astrocytic PERK deletion reduces tau pathology

In addition to amyloid accumulation, tauopathy is a central hallmark of AD.[1] To investigate the role of astrocytic PERK signaling in tau pathology, we utilized PS19 transgenic mice, which express the P301S mutant form of human tau (Figure 5). This model recapitulates key features of tauopathies,[38] including filamentous tau lesions by 6 months, progressive neurofibrillary tangle formation, neuronal loss, and cognitive decline by 8–12 months.[39] At 8 months, PS19 mice exhibited robust activation of the PERK-eIF2α pathway in astrocytes (Figure 5A), accompanied by reduced astrocytic protein synthesis (Figure 5C) and impaired perivascular AQP4 localization (Figures 5D, 5E, and S5). Glymphatic dysfunction in PS19 mice was confirmed using both *in vivo* two-photon imaging and *ex vivo* brain section analysis, which demonstrated reduced CSF tracer influx compared with WT controls (Figures 5F and 5G), consistent with previous reports.[13,40]

To determine whether astrocytic PERK deletion could restore glymphatic function in this model, we crossed PS19 mice with $PERK^{fl/fl}$;$Aldh1l1^{CreER/+}$ mice and administered 4-OHT at 2 months of age (Figure 5B). At 8 months, PERK-deleted PS19 mice (PS19;$PERK^{fl/fl}$;$Aldh1l1^{CreER/+}$) showed enhanced astrocytic protein synthesis (Figure 5C) and improved perivascular AQP4 localization (Figures 5D, 5E, and S5). Glymphatic function was significantly restored, as evidenced by increased CSF tracer penetration into the brain parenchyma in both *in vivo* and *ex vivo* assays (Figures 5F and 5G).

To assess tau pathology, we first examined total phosphorylated tau using the AT8 antibody and found no significant differences between groups in the cortex and hippocampus (Figures 6A, S6A, and S6B). By contrast, levels of pathological tau species detected by MC1 immunostaining were significantly reduced in these regions following astrocytic PERK deletion (Figure 6B), and tau aggregates in the piriform cortex were markedly diminished (Figure 6C). Biochemical analysis further revealed a reduction in the insoluble fraction of total human tau (Figure 6D), accompanied by decreased glial activation in the cortex and hippocampus (Figures S6C and S6D). Behaviorally, PS19 mice with astrocytic PERK deletion exhibited improved spatial memory in the Barnes maze (Figure 6E) and enhanced associative memory in the auditory-cued fear conditioning test (Figure 6F).

Together, these results demonstrate that astrocytic PERK deletion improves glymphatic function, reduces pathological tau accumulation, and alleviates cognitive deficits in PS19 mice, highlighting its therapeutic potential in tauopathies.

PERK activation impairs perivascular AQP4 localization via CK2

Our findings demonstrate that astrocytic PERK deletion enhances perivascular AQP4 localization in both 5XFAD and PS19 mouse models. The phosphorylation and subcellular localization of astrocytic AQP4 are regulated by several intracellular kinases, including protein kinase A (PKA), protein kinase C (PKC), protein kinase G (PKG), and casein kinase 2 (CK2).[41–44] Analysis of snRNA-seq data revealed significant upregulation of *Csnk2a*, which encodes the catalytic α subunit of CK2, in astrocytes from 5XFAD mice compared with WT controls (Figure S7A). Immunofluorescence staining confirmed a ~3-fold increase in CK2α expression in cortical astrocytes of both 5XFAD and PS19 mice relative to WT controls (Figures 7A and 7B). Similarly, elevated CK2α levels were observed in astrocytes from postmortem human AD brain tissue ($p = 0.03$; Figure 7C; Table S1). Notably, astrocytic PERK deletion significantly reduced CK2α expression in both mouse models (Figures 7A and 7B), supporting the hypothesis that PERK activation drives CK2α upregulation in astrocytes, thereby impairing perivascular AQP4 localization.

To directly test this mechanism, we increased CK2 activity in 6-month-old 5XFAD mice lacking astrocytic PERK by administering single or repeated intracisternal injections of exogenous CK2 (10 μM, 10 μL) (Figures 7D and S7B). Compared with vehicle-treated controls, CK2-injected mice exhibited significantly reduced perivascular AQP4 localization 1 to 2 weeks post-injection (Figures 7E and S7B), supporting a causal role for CK2 in AQP4 mislocalization. Conversely, pharmacological inhibition of CK2 with CX-4945 (75 mg/kg intraperitoneally [i.p.], once daily for 1 month) in 5-month-old 5XFAD mice restored perivascular AQP4 localization by 6 months of age (Figures 7F and 7G). CK2 inhibition also enhanced CSF tracer penetration into the brain parenchyma (Figure 7H), reduced Aβ deposition in the cortex and hippocampus (Figure 7I), and improved associative memory performance in the auditory-cued fear conditioning test (Figure 7J). Together, these results

(E) Left, representative brain sections stained with anti-Aβ antibody (6E10) ($n = 6$ mice per group). Right, quantification of Aβ plaque load in the cortex ($p = 0.0147$) and hippocampus ($p = 0.0194$).
(F) Representative navigation paths from the Barnes maze test in 6-month-old WT and 5XFAD mice, with or without astrocytic PERK deletion.
(G) Left, escape latency across 4 training days (days 1–4) in the Barnes maze ($n = 9, 5, 9, 9$ mice). Right, percentage of time spent in the target quadrant during the probe test (day 5) ($p > 0.9999$, $p < 0.0001$, $p = 0.0047$).
(H) Schematic of the auditory-cued fear conditioning paradigm.
(I) Fear response on days 1 and 7 in WT and 5XFAD mice with or without astrocytic PERK deletion ($n = 9, 5, 9, 9$ mice). Day 1, $p > 0.9999$, $p = 0.0002$, $p = 0.0390$; day 7, $p = 0.8512$, $p < 0.0001$, $p = 0.0325$.
Data are presented as mean ± SEM. ns, not significant; $^{*}p < 0.05$, $^{**}p < 0.01$, $^{***}p < 0.001$, $^{****}p < 0.0001$; by one-way ANOVA (G and I) or two-way ANOVA (B–E and G) followed by Bonferroni's test. FC, fold change.
See also Figure S4.

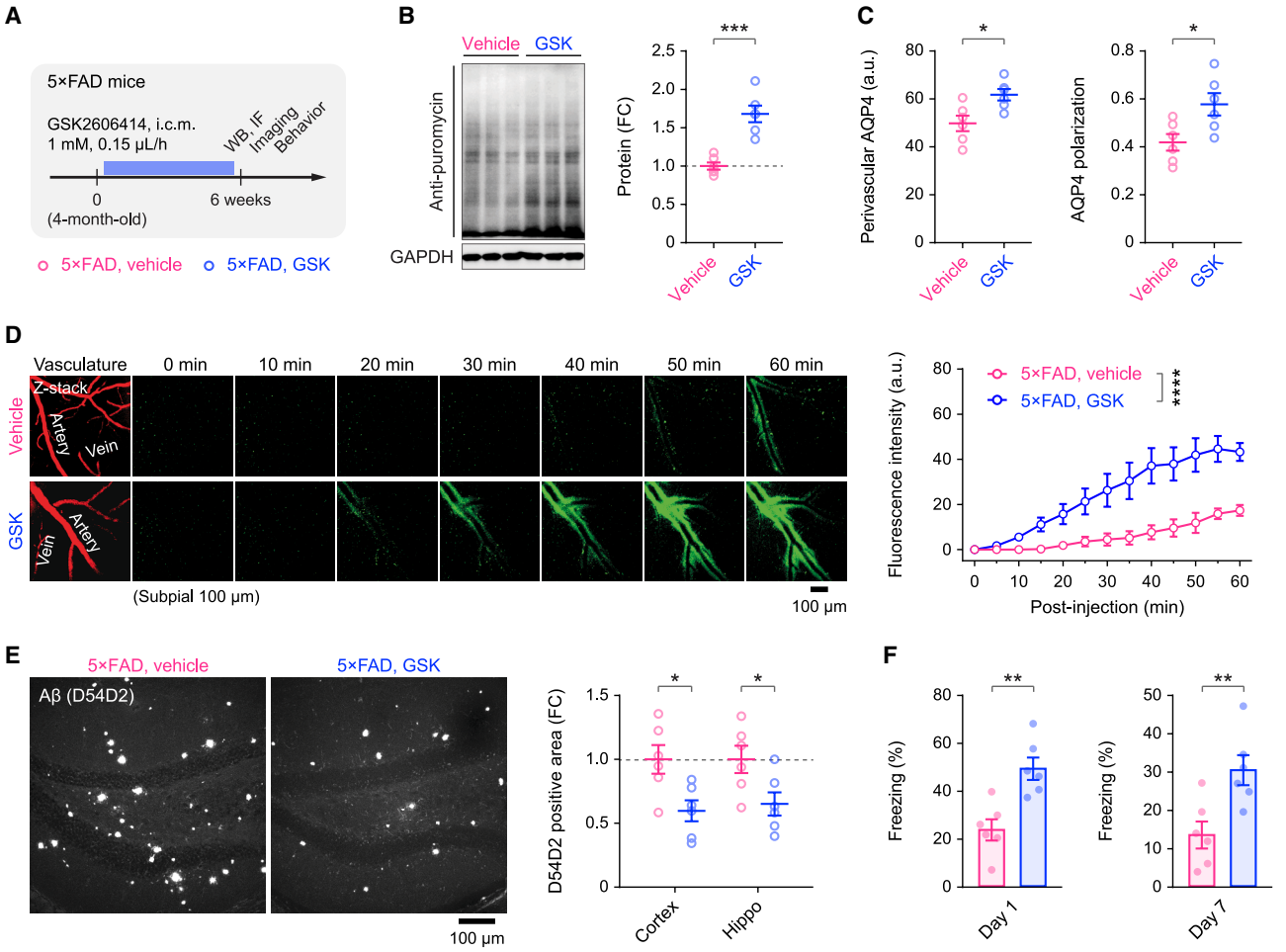

Figure 4. Pharmacological inhibition of PERK improves glymphatic function and mitigates AD pathology in 5XFAD mice

(A) Experimental timeline: 5XFAD mice were treated with vehicle or the PERK inhibitor GSK2606414 (GSK; 1 mM, 0.15 μL/h, i.c.m.) via osmotic minipumps for 6 weeks, followed by various analyses.

(B) Western blot analysis of puromycin-labeled proteins in isolated cortical astrocytes from GSK- or vehicle-treated 5XFAD mice (n = 6 mice per group; p = 0.0002).

(C) Quantification of perivascular AQP4 expression (p = 0.0140) and AQP4 polarization (p = 0.0211) in GSK- versus vehicle-treated 5XFAD mice (n = 6 mice per group).

(D) Left, representative two-photon time-lapse images showing distribution of FITC-dextran tracer in the cortex following intracisternal injection (n = 4, 7 mice). Right, quantification of fluorescence intensity in periarteriolar spaces reveals enhanced CSF tracer influx in GSK-treated 5XFAD mice ($p < 0.0001$).

(E) Left, representative brain sections stained with anti-Aβ antibody (D54D2) (n = 6 mice per group). Right, quantification of Aβ burden in the cortex and hippocampus (p = 0.0183, p = 0.0426).

(F) Auditory-cued fear conditioning test. Freezing behavior on days 1 and 7 post-conditioning in GSK- or vehicle-treated 5XFAD mice (n = 6 mice per group; day 1, p = 0.0026; day 7, p = 0.0092).

Data are presented as mean ± SEM. *$p < 0.05$, **$p < 0.01$, ***$p < 0.001$, ****$p < 0.0001$; by two-tailed unpaired t test (B, C, and F), or two-way ANOVA followed by Bonferroni's test (D and E). FC, fold change; a.u., arbitrary units.

indicate that astrocytic PERK activation impairs glymphatic function and perivascular AQP4 localization through CK2-dependent mechanisms and suggest CK2 as a potential therapeutic target in AD.

DISCUSSION

Impaired glymphatic function has been increasingly implicated in AD,[45] yet the molecular mechanisms driving this dysfunction remain poorly understood. In this study, we demonstrate that astrocytes from both human AD brain tissue and two transgenic mouse models (5XFAD and PS19) exhibit robust activation of the PERK-eIF2α signaling pathway, a key branch of the UPR. In the mouse models, chronic activation of PERK in astrocytes suppresses protein synthesis and disrupts the perivascular localization of AQP4 through CK2-dependent mechanisms (Figure S7C). Genetic deletion or pharmacological inhibition of astrocytic PERK restored glymphatic function, reduced

Please cite this article in press as: Chen et al., Selective removal of astrocytic PERK protects against glymphatic impairment and decreases toxic aggregation of β-amyloid and tau, Neuron (2025), https://doi.org/10.1016/j.neuron.2025.04.027

CellPress

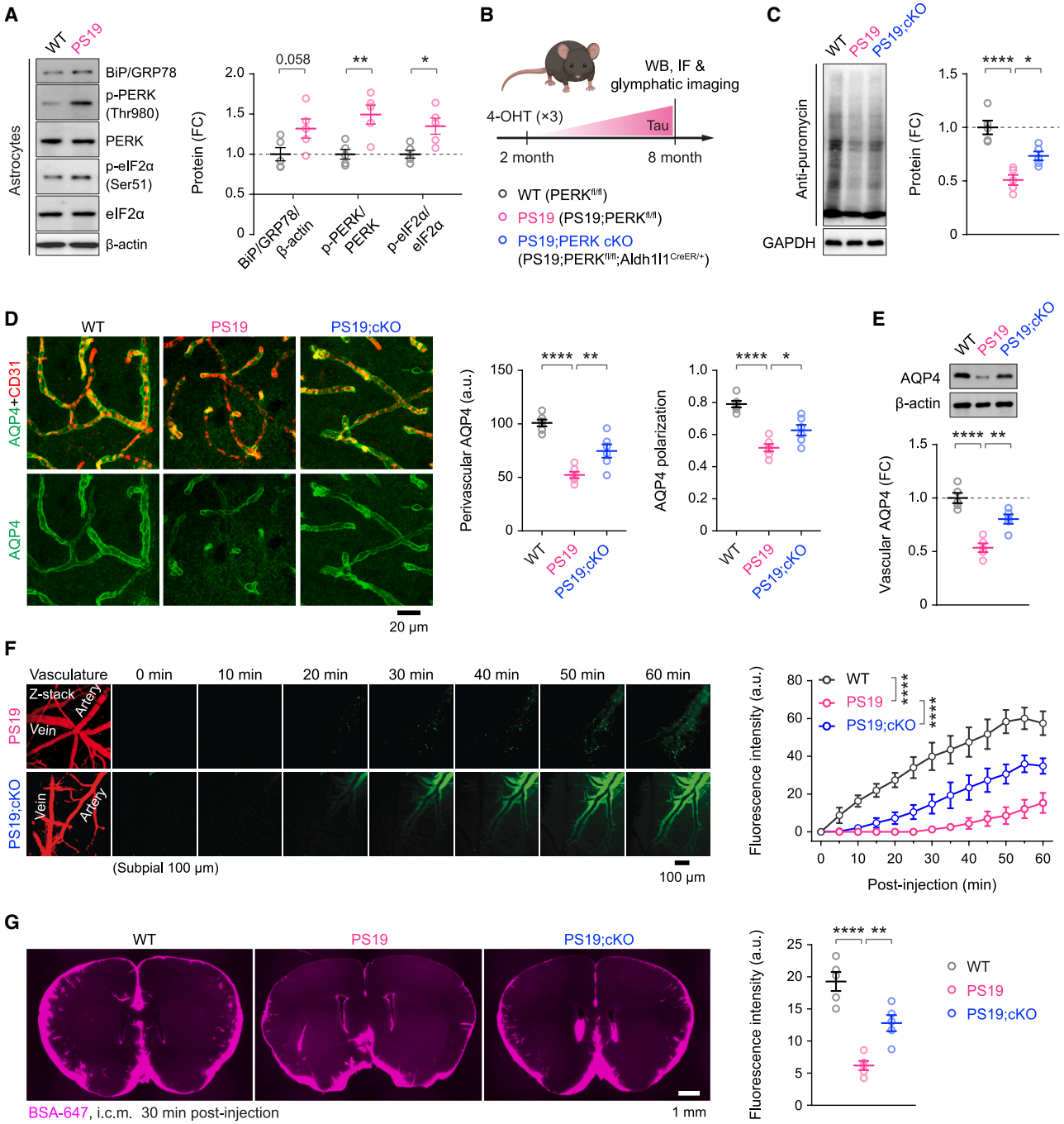

Figure 5. Deletion of astrocytic PERK improves glymphatic function in PS19 mice

(A) Left, western blot analysis of cortical astrocytes isolated from 8-month-old WT and PS19 mice (n = 5 mice per group) using the indicated antibodies. Right, densitometric quantification (p = 0.0585, p = 0.0059, p = 0.0144).

(B) Experimental timeline.

(C) Western blot analysis of puromycin-labeled proteins in cortical astrocytes isolated from WT, PS19, and PERK-deleted PS19 mice (n = 5 mice per group; $p < 0.0001$, p = 0.0203).

(D) Left, representative images of cortical sections immunostained for AQP4 and the vascular marker CD31 (n = 6 mice per group). Right, quantification of perivascular AQP4 expression ($p < 0.0001$, p = 0.0052) and AQP4 polarization ($p < 0.0001$, p = 0.0193).

(E) Western blot analysis of AQP4 protein levels in cerebral vessels isolated from WT, PS19, and PERK-deleted PS19 mice (n = 5 mice per group; $p < 0.0001$, p = 0.0022).

(legend continued on next page)

Please cite this article in press as: Chen et al., Selective removal of astrocytic PERK protects against glymphatic impairment and decreases toxic aggregation of β-amyloid and tau, Neuron (2025), https://doi.org/10.1016/j.neuron.2025.04.027

AD-related pathology, and improved cognitive performance, highlighting astrocytic PERK-eIF2α and CK2 signaling as promising therapeutic targets.

The glymphatic system is a brain-wide perivascular network that facilitates the clearance of metabolic waste and neurotoxic proteins. Using *in vivo* two-photon imaging in mice, Iliff et al. first demonstrated that tracers and solutes can be transported via CSF-ISF exchange in perivascular spaces.[12,25] Subsequent studies have confirmed the presence of this fluid transport pathway in non-human primates and humans using magnetic resonance imaging.[46,47] Current evidence indicates that glymphatic exchange is driven by arterial pulsations,[48–51] facilitated by AQP4 localized to astrocytic endfeet,[12,13,20] and modulated by sleep and circadian rhythms.[52–54] Notably, glymphatic function declines with aging[55,56] and is compromised in several neurodegenerative diseases, including AD,[26,57] Parkinson's disease,[58,59] amyotrophic lateral sclerosis,[60] and multiple sclerosis.[61] Although glymphatic dysfunction may represent an early and common pathological feature across these conditions,[62,63] its therapeutic potential is only beginning to be explored.

Our findings identify astrocytic PERK as a promising target for preserving glymphatic function. Astrocytes, the most abundant glial cells in the brain, play essential roles in maintaining glutamate, ion, and water homeostasis; regulating synaptic transmission; supporting neuronal energy metabolism; and modulating regional blood flow.[64,65] In AD, astrocytes experience ER stress due to the accumulation of misfolded Aβ and tau proteins,[66] leading to activation of UPR signaling and disrupted protein synthesis. Reduced astrocytic protein synthesis has been observed in 3xTg-AD mice,[67] and our data from both 5XFAD and PS19 models indicate that sustained PERK-eIF2α signaling contributes to this suppression. We also detected PERK activation in astrocytes from human AD brain tissue. Importantly, genetic deletion of astrocytic PERK in both 5XFAD and PS19 mice improved perivascular AQP4 localization, restored glymphatic function, reduced toxic protein deposition, and ameliorated cognitive deficits. These beneficial effects were abolished by pharmacological blockade of AQP4, indicating that the therapeutic efficacy of PERK inhibition is mediated, at least in part, by restoring AQP4 localization and function. This is consistent with previous studies demonstrating that glymphatic clearance depends on perivascular AQP4[12,13,20] and that AQP4 loss or mislocalization exacerbates Aβ and tau pathology in AD models.[13,22,23] Nevertheless, the mechanistic link between impaired extracellular tau clearance and intracellular tau aggregation remains incompletely understood. Moreover, as AQP4 mislocalization has also been observed in other amyloid models, such as tg-ArcSwe mice,[68] future studies are warranted to determine whether astrocytic PERK signaling similarly contributes to glymphatic dysfunction across diverse AD pathologies.

We also identified CK2, a constitutively active serine/threonine kinase, as a key mediator of PERK-induced AQP4 mislocalization. Three lines of evidence support this conclusion: (1) CK2α is upregulated in PERK-activated astrocytes in both human AD brain tissue (as shown here and in prior studies[69]) and in transgenic AD mouse models; (2) astrocyte-specific deletion of PERK reduces CK2α expression; and (3) inhibition of either PERK or CK2 restores perivascular AQP4 localization, enhances glymphatic function, and improves cognitive performance. These findings are further supported by a recent report that CK2 inhibition reduces tau pathology in cultured hippocampal neurons derived from AD patients.[70] Although the precise molecular link between PERK and CK2 remains to be fully elucidated, CK2 has been shown to interact with activating transcription factor 4 (ATF4),[71] whose translation is selectively upregulated downstream of the PERK-eIF2α signaling.[72,73] Our snRNA-seq analysis of 5XFAD mouse brains revealed significant upregulation of *Atf4* in astrocytes (Figure 1B). Future studies targeting these downstream effectors will be essential to further clarify the role of PERK-eIF2α-CK2 axis in AQP4 mislocalization and glymphatic dysfunction.

Beyond AQP4 localization, additional mechanisms likely contribute to improved glymphatic function and reduced AD pathology observed following astrocytic PERK deletion. In both 5XFAD and PS19 mice, PERK deletion reduced glial activation in the brain parenchyma. Recent studies have highlighted the role of perivascular macrophages, particularly LYVE1-expressing subsets, in regulating CSF flow dynamics.[34,35] In 5XFAD mice, we observed an increase in $MHCII^{+}CD206^{+}$ parenchyma border macrophages (PBMs) and a reduction in $LYVE1^{+}CD206^{+}$ PBMs compared with WT controls. These alterations were partially reversed by astrocytic PERK deletion, potentially contributing to improved CSF perfusion. Additionally, although astrocytic PERK deletion had no apparent effect on meningeal lymphatic vessel density, it significantly enhanced meningeal lymphatic drainage in 5XFAD mice, as indicated by increased clearance of tracers from the CSF to the dCLNs. These findings support a close interplay between the glymphatic and meningeal lymphatic systems. Consistent with this relationship, previous studies have shown that AQP4 knockout reduces tau clearance to the dCLNs[13] and that disruption of meningeal lymphatics impairs glymphatic flow and AQP4 localization, thereby exacerbating Aβ pathology in AD models.[74,75]

Astrocytes influence AD progression through multiple mechanisms beyond glymphatic regulation.[76] For example, conditional knockout of astrocytic low-density lipoprotein receptor-related protein 1 (LRP1), an endocytic receptor for Aβ, impairs Aβ

(F) Left, representative two-photon time-lapse images showing distribution of FITC-dextran tracer in the cortex following intracisternal injection. Right, quantification of tracer fluorescence intensity in periarteriolar spaces (n = 5, 5, 6 mice; $p < 0.0001$).
(G) Left, representative coronal brain sections showing distribution of BSA-647 tracer 30 min after intracisternal injection (n = 5 mice per group). Right, quantification of tracer fluorescence intensity in the somatosensory cortex ($p < 0.0001$, $p = 0.0042$).
Data are presented as mean ± SEM. *$p < 0.05$, **$p < 0.01$, ****$p < 0.0001$; by two-tailed unpaired t test (A), one-way ANOVA (C–E, and G), or two-way ANOVA (F) followed by Bonferroni's test. FC, fold change; a.u., arbitrary units.
See also Figure S5.

Please cite this article in press as: Chen et al., Selective removal of astrocytic PERK protects against glymphatic impairment and decreases toxic aggregation of β-amyloid and tau, Neuron (2025), https://doi.org/10.1016/j.neuron.2025.04.027

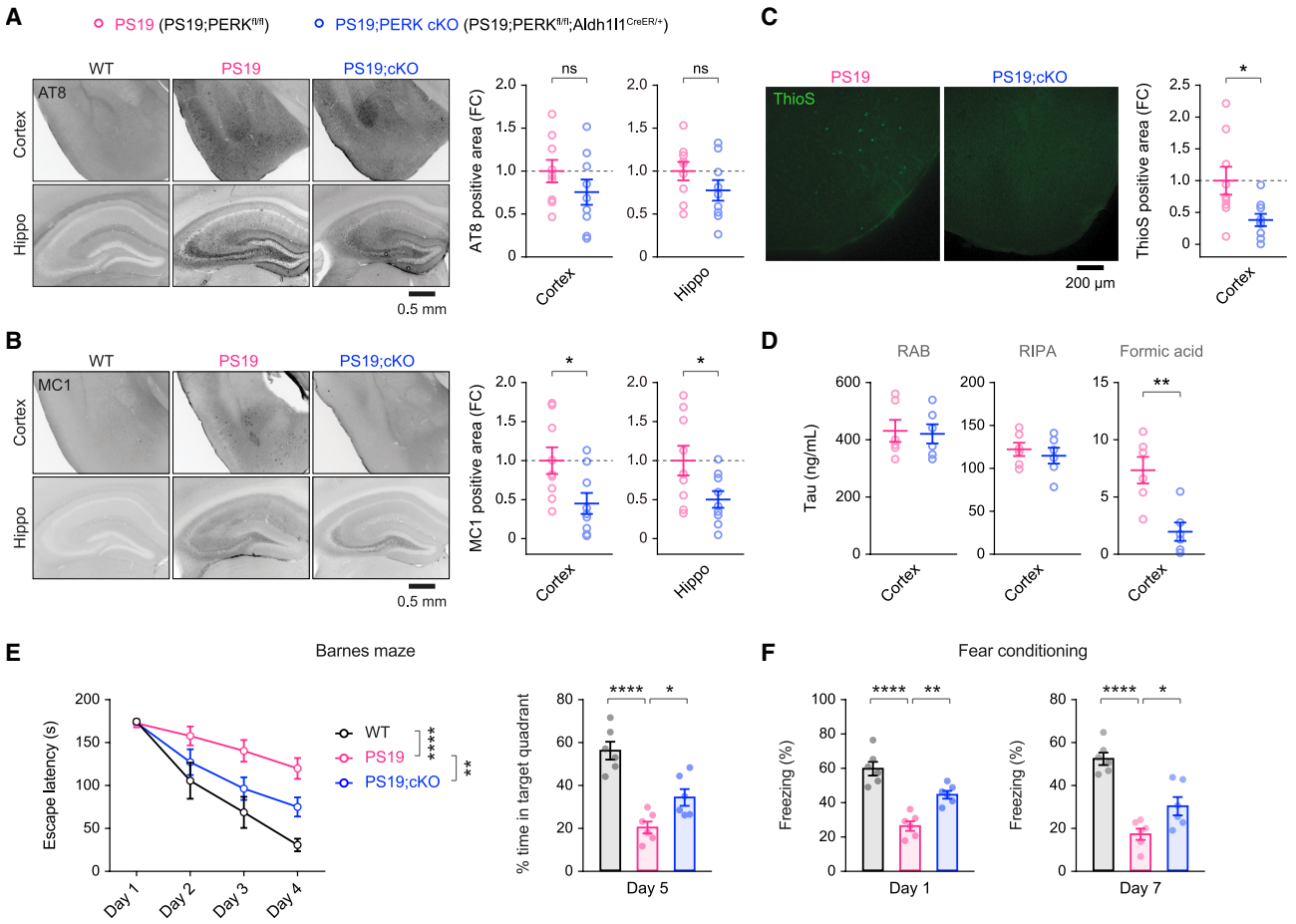

Figure 6. Astrocytic PERK deletion reduces tau pathology and improves memory in PS19 mice

(A) Left, representative brain sections immunostained for phosphorylated tau using AT8 antibody ($n = 9$ mice per group). Right, quantification of AT8-positive area in the piriform cortex ($p = 0.2317$) and hippocampus ($p = 0.1850$).

(B) Left, representative brain sections immunostained for pathological tau using MC1 antibody ($n = 9$ mice per group). Right, quantification of MC1-positive area in the piriform cortex ($p = 0.0221$) and hippocampus ($p = 0.0366$).

(C) Left, representative images of tau aggregates in the piriform cortex stained with thioflavin S (ThioS) ($n = 9$ mice per group). Right, quantification of ThioS-positive area ($p = 0.0203$).

(D) ELISA analysis of human tau in cortical lysates from PS19 mice with or without astrocytic PERK deletion ($n = 6$ mice per group), measured in RAB (soluble, $p = 0.8452$), RIPA (soluble and mildly insoluble, $p = 0.5518$), and formic acid (insoluble, $p = 0.0034$) fractions.

(E) Barnes maze test ($n = 6$ mice per group). Astrocytic PERK deletion improves spatial learning over training days 1–4 ($p = 0.0024$) and enhances performance in the day 5 probe trial ($p = 0.0325$).

(F) Auditory-cued fear conditioning test ($n = 6$ mice per group). Astrocytic PERK deletion improves associative fear memory in PS19 mice on day 1 ($p = 0.0017$) and day 7 ($p = 0.0290$).

Data are presented as mean ± SEM. ns, not significant; $^*p < 0.05$, $^{**}p < 0.01$, $^{****}p < 0.0001$; by two-tailed unpaired t test (A–D), one-way ANOVA (E and F), or two-way ANOVA (E) followed by Bonferroni's test. FC, fold change.

See also Figure S6.

clearance and promotes plaque deposition in APP/PS1 mice,[77] while astrocytic overexpression of clusterin has been shown to reduce Aβ accumulation.[78] Additionally, selective removal of astrocytic apoE4, a major genetic risk factor for late-onset AD, attenuates Aβ pathology in APP/PS1 mice[79] and mitigates tau-mediated neurodegeneration in PS19 mice.[80] Deletion of the circadian clock protein BMAL1 specifically in astrocytes also prevents tau pathology in PS19 mice.[81] Whether these interventions influence glymphatic function remains to be determined. Future single-cell RNA sequencing studies comparing models with and without astrocytic PERK deletion may offer deeper insights into how astrocytic UPR signaling modulates these molecular pathways and intercellular interactions during AD progression.

In summary, our study demonstrates the critical role of astrocytic PERK-eIF2α and CK2 signaling in driving AQP4 mislocalization, glymphatic dysfunction, toxic protein aggregation, and cognitive impairment in both 5XFAD and PS19 mouse models. Although astrocytic PERK inhibition enhances glymphatic exchange, CSF transport also relies on arterial pulsations.[48–51]

Please cite this article in press as: Chen et al., Selective removal of astrocytic PERK protects against glymphatic impairment and decreases toxic aggregation of β-amyloid and tau, Neuron (2025), https://doi.org/10.1016/j.neuron.2025.04.027

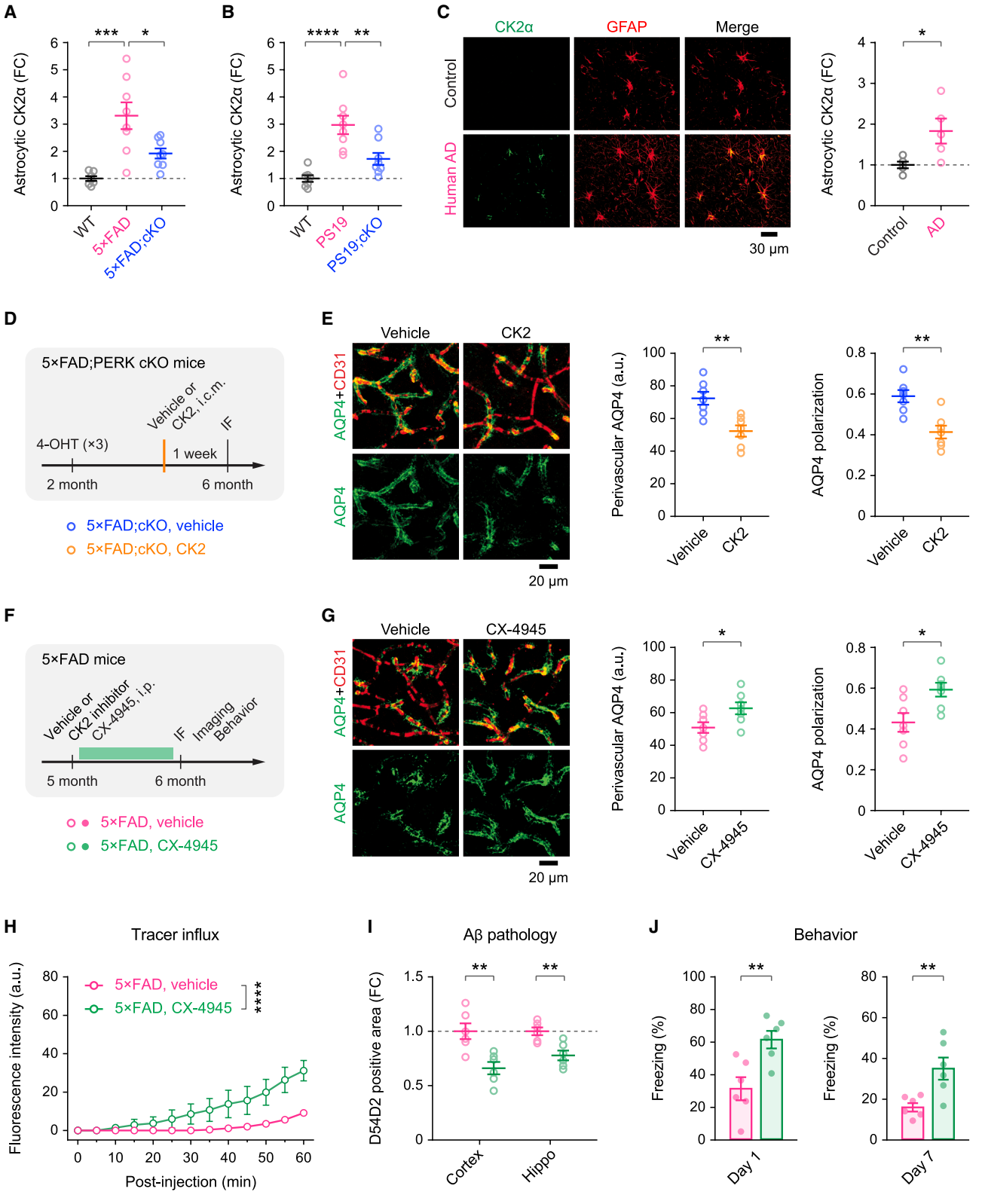

(legend on next page)

Future studies combining PERK inhibitors with vascular modulators, such as angiotensin receptor blockers,[82] may reveal synergistic therapeutic strategies to improve glymphatic clearance and mitigate cognitive decline in AD.

RESOURCE AVAILABILITY

Lead contact

Further information and request for resources and reagents should be directed to and will be fulfilled by the lead contact, Guang Yang (gy2268@cumc.columbia.edu).

Materials availability

This study did not generate new, unique reagents.

Data and code availability

- Data reported in this paper will be shared by the lead contact upon request.
- This paper does not report any original code.
- Any additional information required to reanalyze the data reported in this work paper is available from the lead contact upon request.

ACKNOWLEDGMENTS

We thank members of the Yang lab for their valuable discussions and input. This work was supported by the US National Institutes of Health (AG041274).

AUTHOR CONTRIBUTIONS

Conceptualization, K.C., Y.M.M., Z.X., and G.Y.; methodology, K.C., Y.M.M., T.N., O.A.-D., Z.X., and G.Y.; investigation, K.C., Y.M.M., T.N., and O.A.-D.; visualization, K.C., Z.X., and G.Y.; funding acquisition, Z.X. and G.Y.; writing – original draft, K.C. and G.Y.; writing – review and editing, K.C., Y.M.M., T.N., O.A.-D., Z.X., and G.Y.; supervision, Z.X. and G.Y.

DECLARATION OF INTERESTS

Z.X. provided consulting services within the past 36 months to Baxter; NanoMosaic; Shanghai Fourth, Ninth, and Tenth Hospitals; the Shanghai Mental Health Center affiliated with Shanghai Jiao Tong University School of Medicine; and the journal *Anesthesiology and Perioperative Science*, but he is not currently engaged in any of these roles.

STAR★METHODS

Detailed methods are provided in the online version of this paper and include the following:

- KEY RESOURCES TABLE
- EXPERIMENTAL MODEL AND STUDY PARTICIPANT DETAILS
  - Animals
  - Human post-mortem brain tissue
- METHOD DETAILS
  - Analysis of snRNA-seq data
  - RNA *in situ* hybridization
  - Immunofluorescence and immunohistochemistry
  - Confocal and widefield microscopy
  - Isolation of astrocytes
  - Isolation of brain vessels
  - Western blot
  - Measurement of *de novo* protein synthesis
  - AQP4 expression and polarization analysis
  - Thinned-skull cranial window
  - Cisterna magna cannulation
  - CSF tracers and drugs
  - Two-photon imaging of CSF tracer and analysis
  - *Ex vivo* imaging of CSF tracer and analysis
  - ELISA
  - Behavior
- QUANTIFICATION AND STATISTIAL ANALYSIS

SUPPLEMENTAL INFORMATION

Supplemental information can be found online at https://doi.org/10.1016/j.neuron.2025.04.027.

Received: May 3, 2024
Revised: January 2, 2025
Accepted: April 25, 2025
Published: May 21, 2025

REFERENCES

1. Long, J.M., and Holtzman, D.M. (2019). Alzheimer Disease: An Update on Pathobiology and Treatment Strategies. Cell *179*, 312–339. https://doi.org/10.1016/j.cell.2019.09.001.

Figure 7. Astrocytic PERK activation disrupts perivascular AQP4 localization via CK2

(A) Quantification of CK2α immunoreactivity in cortical astrocytes of 5XFAD mice with or without astrocytic PERK deletion ($n = 7, 8, 8$ mice per group; $p = 0.0001$, $p = 0.0106$).
(B) Quantification of CK2α immunoreactivity in cortical astrocytes of PS19 mice with or without astrocytic PERK deletion ($n = 7, 8, 8$ mice per group; $p < 0.0001$, $p = 0.0039$).
(C) Left, representative images of post-mortem human anterior cingulate cortex stained for GFAP and CK2α from control and AD individuals ($n = 5$ per group). Right, quantification of CK2α immunoreactivity in GFAP-positive astrocytes ($p = 0.0302$).
(D) Experimental timeline for intracisternal administration of CK2 (10 μM, 10 μL, single injection) in PERK-deleted 5XFAD mice.
(E) Left, representative images of cortical sections immunostained for AQP4 and CD31 ($n = 7$ mice per group). Right, quantification of perivascular AQP4 expression ($p = 0.0025$) and polarization ($p = 0.0015$) following CK2 or vehicle administration.
(F) Experimental timeline for pharmacological CK2 inhibition using CX-4945 in 5XFAD mice.
(G) Left, representative images of cortical sections immunostained for AQP4 and CD31 ($n = 7$ mice per group). Right, quantification of perivascular AQP4 expression ($p = 0.0332$) and polarization ($p = 0.0158$) in vehicle- versus CX-4945-treated 5XFAD mice.
(H) Quantification of FITC-dextran tracer intensity in periarteriolar spaces following intracisternal injection. CX-4945 treatment significantly enhances tracer influx compared with vehicle controls ($n = 4, 6$ mice; $p < 0.0001$).
(I) Quantification of Aβ plaque burden in the cortex ($p = 0.0043$) and hippocampus ($p = 0.0031$) of vehicle- and CX-4945-treated 5XFAD mice ($n = 6$ mice per group).
(J) Auditory-cued fear conditioning test ($n = 6$ mice per group). CX-4945 treatment improves fear memory performance in 5XFAD mice (day 1, $p = 0.0068$; day 7, $p = 0.0085$).
Data are presented as mean ± SEM. $^{*}p < 0.05$, $^{**}p < 0.01$, $^{***}p < 0.001$, $^{****}p < 0.0001$; by two-tailed unpaired t test (C, E, G, I, and J), one-way ANOVA (A and B), or two-way ANOVA (H) followed by Bonferroni's test. FC, fold change; a.u., arbitrary units.
See also Figure S7 and Table S1.

2. Lane, C.A., Hardy, J., and Schott, J.M. (2018). Alzheimer's disease. Eur. J. Neurol. *25*, 59–70. https://doi.org/10.1111/ene.13439.

3. Hetz, C. (2012). The unfolded protein response: controlling cell fate decisions under ER stress and beyond. Nat. Rev. Mol. Cell Biol. *13*, 89–102. https://doi.org/10.1038/nrm3270.

4. Hetz, C., Zhang, K., and Kaufman, R.J. (2020). Mechanisms, regulation and functions of the unfolded protein response. Nat. Rev. Mol. Cell Biol. *21*, 421–438. https://doi.org/10.1038/s41580-020-0250-z.

5. Ma, T., Trinh, M.A., Wexler, A.J., Bourbon, C., Gatti, E., Pierre, P., Cavener, D.R., and Klann, E. (2013). Suppression of eIF2alpha kinases alleviates Alzheimer's disease-related plasticity and memory deficits. Nat. Neurosci. *16*, 1299–1305. https://doi.org/10.1038/nn.3486.

6. Radford, H., Moreno, J.A., Verity, N., Halliday, M., and Mallucci, G.R. (2015). PERK inhibition prevents tau-mediated neurodegeneration in a mouse model of frontotemporal dementia. Acta Neuropathol. *130*, 633–642. https://doi.org/10.1007/s00401-015-1487-z.

7. Hughes, D., and Mallucci, G.R. (2019). The unfolded protein response in neurodegenerative disorders - therapeutic modulation of the PERK pathway. FEBS Journal *286*, 342–355. https://doi.org/10.1111/febs.14422.

8. Scheper, W., and Hoozemans, J.J.M. (2015). The unfolded protein response in neurodegenerative diseases: a neuropathological perspective. Acta Neuropathol. *130*, 315–331. https://doi.org/10.1007/s00401-015-1462-8.

9. Hetz, C., and Saxena, S. (2017). ER stress and the unfolded protein response in neurodegeneration. Nat. Rev. Neurol. *13*, 477–491. https://doi.org/10.1038/nrneurol.2017.99.

10. Smith, H.L., Freeman, O.J., Butcher, A.J., Holmqvist, S., Humoud, I., Schätzl, T., Hughes, D.T., Verity, N.C., Swinden, D.P., Hayes, J., et al. (2020). Astrocyte Unfolded Protein Response Induces a Specific Reactivity State that Causes Non-Cell-Autonomous Neuronal Degeneration. Neuron *105*, 855–866.e5. https://doi.org/10.1016/j.neuron.2019.12.014.

11. Rennels, M.L., Gregory, T.F., Blaumanis, O.R., Fujimoto, K., and Grady, P. A. (1985). Evidence for a 'paravascular' fluid circulation in the mammalian central nervous system, provided by the rapid distribution of tracer protein throughout the brain from the subarachnoid space. Brain Res. *326*, 47–63. https://doi.org/10.1016/0006-8993(85)91383-6.

12. Iliff, J.J., Wang, M., Liao, Y., Plogg, B.A., Peng, W., Gundersen, G.A., Benveniste, H., Vates, G.E., Deane, R., Goldman, S.A., et al. (2012). A paravascular pathway facilitates CSF flow through the brain parenchyma and the clearance of interstitial solutes, including amyloid β. Sci. Transl. Med. *4*, 147ra111. https://doi.org/10.1126/scitranslmed.3003748.

13. Ishida, K., Yamada, K., Nishiyama, R., Hashimoto, T., Nishida, I., Abe, Y., Yasui, M., and Iwatsubo, T. (2022). Glymphatic system clears extracellular tau and protects from tau aggregation and neurodegeneration. J. Exp. Med. *219*, e20211275. https://doi.org/10.1084/jem.20211275.

14. Murdock, M.H., Yang, C.Y., Sun, N., Pao, P.C., Blanco-Duque, C., Kahn, M.C., Kim, T., Lavoie, N.S., Victor, M.B., Islam, M.R., et al. (2024). Multisensory gamma stimulation promotes glymphatic clearance of amyloid. Nature *627*, 149–156. https://doi.org/10.1038/s41586-024-07132-6.

15. Jiang-Xie, L.F., Drieu, A., Bhasiin, K., Quintero, D., Smirnov, I., and Kipnis, J. (2024). Neuronal dynamics direct cerebrospinal fluid perfusion and brain clearance. Nature *627*, 157–164. https://doi.org/10.1038/s41586-024-07108-6.

16. Aspelund, A., Antila, S., Proulx, S.T., Karlsen, T.V., Karaman, S., Detmar, M., Wiig, H., and Alitalo, K. (2015). A dural lymphatic vascular system that drains brain interstitial fluid and macromolecules. J. Exp. Med. *212*, 991–999. https://doi.org/10.1084/jem.20142290.

17. Louveau, A., Smirnov, I., Keyes, T.J., Eccles, J.D., Rouhani, S.J., Peske, J. D., Derecki, N.C., Castle, D., Mandell, J.W., Lee, K.S., et al. (2015). Structural and functional features of central nervous system lymphatic vessels. Nature *523*, 337–341. https://doi.org/10.1038/nature14432.

18. Ahn, J.H., Cho, H., Kim, J.H., Kim, S.H., Ham, J.S., Park, I., Suh, S.H., Hong, S.P., Song, J.H., Hong, Y.K., et al. (2019). Meningeal lymphatic vessels at the skull base drain cerebrospinal fluid. Nature *572*, 62–66. https://doi.org/10.1038/s41586-019-1419-5.

19. Smyth, L.C.D., Xu, D., Okar, S.V., Dykstra, T., Rustenhoven, J., Papadopoulos, Z., Bhasiin, K., Kim, M.W., Drieu, A., Mamuladze, T., et al. (2024). Identification of direct connections between the dura and the brain. Nature *627*, 165–173. https://doi.org/10.1038/s41586-023-06993-7.

20. Mestre, H., Hablitz, L.M., Xavier, A.L., Feng, W., Zou, W., Pu, T., Monai, H., Murlidharan, G., Castellanos Rivera, R.M., Simon, M.J., et al. (2018). Aquaporin-4-dependent glymphatic solute transport in the rodent brain. eLife *7*, e40070. https://doi.org/10.7554/eLife.40070.

21. Neely, J.D., Amiry-Moghaddam, M., Ottersen, O.P., Froehner, S.C., Agre, P., and Adams, M.E. (2001). Syntrophin-dependent expression and localization of Aquaporin-4 water channel protein. Proc. Natl. Acad. Sci. USA *98*, 14108–14113. https://doi.org/10.1073/pnas.241508198.

22. Xu, Z., Xiao, N., Chen, Y., Huang, H., Marshall, C., Gao, J., Cai, Z., Wu, T., Hu, G., and Xiao, M. (2015). Deletion of aquaporin-4 in APP/PS1 mice exacerbates brain Abeta accumulation and memory deficits. Mol. Neurodegener. *10*, 58. https://doi.org/10.1186/s13024-015-0056-1.

23. Pedersen, T.J., Keil, S.A., Han, W., Wang, M.X., and Iliff, J.J. (2023). The effect of aquaporin-4 mis-localization on Abeta deposition in mice. Neurobiol. Dis. *181*, 106100. https://doi.org/10.1016/j.nbd.2023.106100.

24. Mestre, H., Du, T., Sweeney, A.M., Liu, G., Samson, A.J., Peng, W., Mortensen, K.N., Stæger, F.F., Bork, P.A.R., Bashford, L., et al. (2020). Cerebrospinal fluid influx drives acute ischemic tissue swelling. Science *367*, eaax7171. https://doi.org/10.1126/science.aax7171.

25. Iliff, J.J., Chen, M.J., Plog, B.A., Zeppenfeld, D.M., Soltero, M., Yang, L., Singh, I., Deane, R., and Nedergaard, M. (2014). Impairment of glymphatic pathway function promotes tau pathology after traumatic brain injury. J. Neurosci. *34*, 16180–16193. https://doi.org/10.1523/JNEUROSCI.3020-14.2014.

26. Zeppenfeld, D.M., Simon, M., Haswell, J.D., D'Abreo, D., Murchison, C., Quinn, J.F., Grafe, M.R., Woltjer, R.L., Kaye, J., and Iliff, J.J. (2017). Association of Perivascular Localization of Aquaporin-4 With Cognition and Alzheimer Disease in Aging Brains. JAMA Neurol. *74*, 91–99. https://doi.org/10.1001/jamaneurol.2016.4370.

27. Simon, M.J., Wang, M.X., Murchison, C.F., Roese, N.E., Boespflug, E.L., Woltjer, R.L., and Iliff, J.J. (2018). Transcriptional network analysis of human astrocytic endfoot genes reveals region-specific associations with dementia status and tau pathology. Sci. Rep. *8*, 12389. https://doi.org/10.1038/s41598-018-30779-x.

28. Zhou, Y., Song, W.M., Andhey, P.S., Swain, A., Levy, T., Miller, K.R., Poliani, P.L., Cominelli, M., Grover, S., Gilfillan, S., et al. (2020). Human and mouse single-nucleus transcriptomics reveal TREM2-dependent and TREM2-independent cellular responses in Alzheimer's disease. Nat. Med. *26*, 131–142. https://doi.org/10.1038/s41591-019-0695-9.

29. Srinivasan, R., Lu, T.Y., Chai, H., Xu, J., Huang, B.S., Golshani, P., Coppola, G., and Khakh, B.S. (2016). New Transgenic Mouse Lines for Selectively Targeting Astrocytes and Studying Calcium Signals in Astrocyte Processes In Situ and In Vivo. Neuron *92*, 1181–1195. https://doi.org/10.1016/j.neuron.2016.11.030.

30. Zhang, P., McGrath, B., Li, S., Frank, A., Zambito, F., Reinert, J., Gannon, M., Ma, K., McNaughton, K., and Cavener, D.R. (2002). The PERK eukaryotic initiation factor 2 alpha kinase is required for the development of the skeletal system, postnatal growth, and the function and viability of the pancreas. Mol. Cell. Biol. *22*, 3864–3874. https://doi.org/10.1128/MCB.22.11.3864-3874.2002.

31. Wolzak, K., Nölle, A., Farina, M., Abbink, T.E., van der Knaap, M.S., Verhage, M., and Scheper, W. (2022). Neuron-specific translational control shift ensures proteostatic resilience during ER stress. EMBO J. *41*, e110501. https://doi.org/10.15252/embj.2021110501.

32. Shrestha, P., Shan, Z., Mamcarz, M., Ruiz, K.S.A., Zerihoun, A.T., Juan, C. Y., Herrero-Vidal, P.M., Pelletier, J., Heintz, N., and Klann, E. (2020). Amygdala inhibitory neurons as loci for translation in emotional memories. Nature *586*, 407–411. https://doi.org/10.1038/s41586-020-2793-8.

33. Oakley, H., Cole, S.L., Logan, S., Maus, E., Shao, P., Craft, J., Guillozet-Bongaarts, A., Ohno, M., Disterhoft, J., Van Eldik, L., et al. (2006). Intraneuronal beta-amyloid aggregates, neurodegeneration, and neuron loss in transgenic mice with five familial Alzheimer's disease mutations: potential factors in amyloid plaque formation. J. Neurosci. *26*, 10129–10140. https://doi.org/10.1523/JNEUROSCI.1202-06.2006.

34. Drieu, A., Du, S., Storck, S.E., Rustenhoven, J., Papadopoulos, Z., Dykstra, T., Zhong, F., Kim, K., Blackburn, S., Mamuladze, T., et al. (2022). Parenchymal border macrophages regulate the flow dynamics of the cerebrospinal fluid. Nature *611*, 585–593. https://doi.org/10.1038/s41586-022-05397-3.

35. Drieu, A., Du, S., Kipnis, M., Bosch, M.E., Herz, J., Lee, C., Jiang, H., Manis, M., Ulrich, J.D., Kipnis, J., et al. (2023). Parenchymal border macrophages regulate tau pathology and tau-mediated neurodegeneration. Life Sci. Alliance *6*, e202302087. https://doi.org/10.26508/lsa.202302087.

36. Chen, K., Gupta, R., Martín-Ávila, A., Cui, M., Xie, Z., and Yang, G. (2024). Anesthesia-induced hippocampal-cortical hyperactivity and tau hyperphosphorylation impair remote memory retrieval in Alzheimer's disease. Alzheimers Dement. *20*, 494–510. https://doi.org/10.1002/alz.13464.

37. Moreno, J.A., Halliday, M., Molloy, C., Radford, H., Verity, N., Axten, J.M., Ortori, C.A., Willis, A.E., Fischer, P.M., Barrett, D.A., and Mallucci, G.R. (2013). Oral treatment targeting the unfolded protein response prevents neurodegeneration and clinical disease in prion-infected mice. Sci. Transl. Med. *5*, 206ra138. https://doi.org/10.1126/scitranslmed.3006767.

38. Iqbal, K., Liu, F., Gong, C.X., and Grundke-Iqbal, I. (2010). Tau in Alzheimer disease and related tauopathies. Curr. Alzheimer Res. *7*, 656–664. https://doi.org/10.2174/156720510793611592.

39. Yoshiyama, Y., Higuchi, M., Zhang, B., Huang, S.M., Iwata, N., Saido, T.C., Maeda, J., Suhara, T., Trojanowski, J.Q., and Lee, V.M.Y. (2007). Synapse loss and microglial activation precede tangles in a P301S tauopathy mouse model. Neuron *53*, 337–351. https://doi.org/10.1016/j.neuron.2007.01.010.

40. Harrison, I.F., Ismail, O., Machhada, A., Colgan, N., Ohene, Y., Nahavandi, P., Ahmed, Z., Fisher, A., Meftah, S., Murray, T.K., et al. (2020). Impaired glymphatic function and clearance of tau in an Alzheimer's disease model. Brain *143*, 2576–2593. https://doi.org/10.1093/brain/awaa179.

41. Kadohira, I., Abe, Y., Nuriya, M., Sano, K., Tsuji, S., Arimitsu, T., Yoshimura, Y., and Yasui, M. (2008). Phosphorylation in the C-terminal domain of Aquaporin-4 is required for Golgi transition in primary cultured astrocytes. Biochem. Biophys. Res. Commun. *377*, 463–468. https://doi.org/10.1016/j.bbrc.2008.09.155.

42. Nesverova, V., and Törnroth-Horsefield, S. (2019). Phosphorylation-Dependent Regulation of Mammalian Aquaporins. Cells *8*, 82. https://doi.org/10.3390/cells8020082.

43. Vandebroek, A., and Yasui, M. (2020). Regulation of AQP4 in the Central Nervous System. Int. J. Mol. Sci. *21*, 1603. https://doi.org/10.3390/ijms21051603.

44. Kitchen, P., Salman, M.M., Halsey, A.M., Clarke-Bland, C., MacDonald, J. A., Ishida, H., Vogel, H.J., Almutiri, S., Logan, A., Kreida, S., et al. (2020). Targeting Aquaporin-4 Subcellular Localization to Treat Central Nervous System Edema. Cell *181*, 784–799.e19. https://doi.org/10.1016/j.cell.2020.03.037.

45. Rasmussen, M.K., Mestre, H., and Nedergaard, M. (2018). The glymphatic pathway in neurological disorders. Lancet Neurol. *17*, 1016–1024. https://doi.org/10.1016/S1474-4422(18)30318-1.

46. Goulay, R., Flament, J., Gauberti, M., Naveau, M., Pasquet, N., Gakuba, C., Emery, E., Hantraye, P., Vivien, D., Aron-Badin, R., and Gaberel, T. (2017). Subarachnoid Hemorrhage Severely Impairs Brain Parenchymal Cerebrospinal Fluid Circulation in Nonhuman Primate. Stroke *48*, 2301–2305. https://doi.org/10.1161/STROKEAHA.117.017014.

47. Ringstad, G., Vatnehol, S.A.S., and Eide, P.K. (2017). Glymphatic MRI in idiopathic normal pressure hydrocephalus. Brain *140*, 2691–2705. https://doi.org/10.1093/brain/awx191.

48. Iliff, J.J., Wang, M., Zeppenfeld, D.M., Venkataraman, A., Plog, B.A., Liao, Y., Deane, R., and Nedergaard, M. (2013). Cerebral arterial pulsation drives paravascular CSF-interstitial fluid exchange in the murine brain. J. Neurosci. *33*, 18190–18199. https://doi.org/10.1523/JNEUROSCI.1592-13.2013.

49. Mestre, H., Tithof, J., Du, T., Song, W., Peng, W., Sweeney, A.M., Olveda, G., Thomas, J.H., Nedergaard, M., and Kelley, D.H. (2018). Flow of cerebrospinal fluid is driven by arterial pulsations and is reduced in hypertension. Nat. Commun. *9*, 4878. https://doi.org/10.1038/s41467-018-07318-3.

50. van Veluw, S.J., Hou, S.S., Calvo-Rodriguez, M., Arbel-Ornath, M., Snyder, A.C., Frosch, M.P., Greenberg, S.M., and Bacskai, B.J. (2020). Vasomotion as a Driving Force for Paravascular Clearance in the Awake Mouse Brain. Neuron *105*, 549–561.e5. https://doi.org/10.1016/j.neuron.2019.10.033.

51. Hauglund, N.L., Andersen, M., Tokarska, K., Radovanovic, T., Kjaerby, C., Sørensen, F.L., Bojarowska, Z., Untiet, V., Ballestero, S.B., Kolmos, M.G., et al. (2025). Norepinephrine-mediated slow vasomotion drives glymphatic clearance during sleep. Cell *188*, 606–622.e17. https://doi.org/10.1016/j.cell.2024.11.027.

52. Xie, L., Kang, H., Xu, Q., Chen, M.J., Liao, Y., Thiyagarajan, M., O'Donnell, J., Christensen, D.J., Nicholson, C., Iliff, J.J., et al. (2013). Sleep drives metabolite clearance from the adult brain. Science *342*, 373–377. https://doi.org/10.1126/science.1241224.

53. Miao, A., Luo, T., Hsieh, B., Edge, C.J., Gridley, M., Wong, R.T.C., Constandinou, T.G., Wisden, W., and Franks, N.P. (2024). Brain clearance is reduced during sleep and anesthesia. Nat. Neurosci. *27*, 1046–1050. https://doi.org/10.1038/s41593-024-01638-y.

54. Hablitz, L.M., Plá, V., Giannetto, M., Vinitsky, H.S., Stæger, F.F., Metcalfe, T., Nguyen, R., Benrais, A., and Nedergaard, M. (2020). Circadian control of brain glymphatic and lymphatic fluid flow. Nat. Commun. *11*, 4411. https://doi.org/10.1038/s41467-020-18115-2.

55. Kress, B.T., Iliff, J.J., Xia, M., Wang, M., Wei, H.S., Zeppenfeld, D., Xie, L., Kang, H., Xu, Q., Liew, J.A., et al. (2014). Impairment of paravascular clearance pathways in the aging brain. Ann. Neurol. *76*, 845–861. https://doi.org/10.1002/ana.24271.

56. Hsiao, W.C., Chang, H.I., Hsu, S.W., Lee, C.C., Huang, S.H., Cheng, C.H., Huang, C.W., and Chang, C.C. (2023). Association of Cognition and Brain Reserve in Aging and Glymphatic Function Using Diffusion Tensor Image-along the Perivascular Space (DTI-ALPS). Neuroscience *524*, 11–20. https://doi.org/10.1016/j.neuroscience.2023.04.004.

57. Taoka, T., Masutani, Y., Kawai, H., Nakane, T., Matsuoka, K., Yasuno, F., Kishimoto, T., and Naganawa, S. (2017). Evaluation of glymphatic system activity with the diffusion MR technique: diffusion tensor image analysis along the perivascular space (DTI-ALPS) in Alzheimer's disease cases. Jpn. J. Radiol. *35*, 172–178. https://doi.org/10.1007/s11604-017-0617-z.

58. McKnight, C.D., Trujillo, P., Lopez, A.M., Petersen, K., Considine, C., Lin, Y.C., Yan, Y., Kang, H., Donahue, M.J., and Claassen, D.O. (2021). Diffusion along perivascular spaces reveals evidence supportive of glymphatic function impairment in Parkinson disease. Parkinsonism Relat. Disord. *89*, 98–104. https://doi.org/10.1016/j.parkreldis.2021.06.004.

59. Shen, T., Yue, Y., Ba, F., He, T., Tang, X., Hu, X., Pu, J., Huang, C., Lv, W., Zhang, B., et al. (2022). Diffusion along perivascular spaces as marker for impairment of glymphatic system in Parkinson's disease. npj Parkinsons Dis. *8*, 174. https://doi.org/10.1038/s41531-022-00437-1.

60. Liu, S., Sun, X., Ren, Q., Chen, Y., Dai, T., Yang, Y., Gong, G., Li, W., Zhao, Y., Meng, X., et al. (2024). Glymphatic dysfunction in patients with early-stage amyotrophic lateral sclerosis. Brain *147*, 100–108. https://doi.org/10.1093/brain/awad274.

61. Carotenuto, A., Cacciaguerra, L., Pagani, E., Preziosa, P., Filippi, M., and Rocca, M.A. (2022). Glymphatic system impairment in multiple sclerosis:

relation with brain damage and disability. Brain *145*, 2785–2795. https://doi.org/10.1093/brain/awab454.

62. Boland, B., Yu, W.H., Corti, O., Mollereau, B., Henriques, A., Bezard, E., Pastores, G.M., Rubinsztein, D.C., Nixon, R.A., Duchen, M.R., et al. (2018). Promoting the clearance of neurotoxic proteins in neurodegenerative disorders of ageing. Nat. Rev. Drug Discov. *17*, 660–688. https://doi.org/10.1038/nrd.2018.109.

63. Nedergaard, M., and Goldman, S.A. (2020). Glymphatic failure as a final common pathway to dementia. Science *370*, 50–56. https://doi.org/10.1126/science.abb8739.

64. Beard, E., Lengacher, S., Dias, S., Magistretti, P.J., and Finsterwald, C. (2021). Astrocytes as Key Regulators of Brain Energy Metabolism: New Therapeutic Perspectives. Front. Physiol. *12*, 825816. https://doi.org/10.3389/fphys.2021.825816.

65. Bélanger, M., Allaman, I., and Magistretti, P.J. (2011). Brain energy metabolism: focus on astrocyte-neuron metabolic cooperation. Cell Metab. *14*, 724–738. https://doi.org/10.1016/j.cmet.2011.08.016.

66. Acosta, C., Anderson, H.D., and Anderson, C.M. (2017). Astrocyte dysfunction in Alzheimer disease. J. Neurosci. Res. *95*, 2430–2447. https://doi.org/10.1002/jnr.24075.

67. Tapella, L., Dematteis, G., Moro, M., Pistolato, B., Tonelli, E., Vanella, V.V., Giustina, D., La Forgia, A., Restelli, E., Barberis, E., et al. (2022). Protein synthesis inhibition and loss of homeostatic functions in astrocytes from an Alzheimer's disease mouse model: a role for ER-mitochondria interaction. Cell Death Dis. *13*, 878. https://doi.org/10.1038/s41419-022-05324-4.

68. Yang, J., Lunde, L.K., Nuntagij, P., Oguchi, T., Camassa, L.M.A., Nilsson, L.N.G., Lannfelt, L., Xu, Y., Amiry-Moghaddam, M., Ottersen, O.P., et al. (2011). Loss of astrocyte polarization in the tg-ArcSwe mouse model of Alzheimer's disease. J. Alzheimers Dis. *27*, 711–722. https://doi.org/10.3233/JAD-2011-110725.

69. Rosenberger, A.F.N., Morrema, T.H.J., Gerritsen, W.H., van Haastert, E. S., Snkhchyan, H., Hilhorst, R., Rozemuller, A.J.M., Scheltens, P., van der Vies, S.M., and Hoozemans, J.J.M. (2016). Increased occurrence of protein kinase CK2 in astrocytes in Alzheimer's disease pathology. J. Neuroinflammation *13*, 4. https://doi.org/10.1186/s12974-015-0470-x.

70. Marshall, C.A., McBride, J.D., Changolkar, L., Riddle, D.M., Trojanowski, J.Q., and Lee, V.M.Y. (2022). Inhibition of CK2 mitigates Alzheimer's tau pathology by preventing NR2B synaptic mislocalization. Acta Neuropathol. Commun. *10*, 30. https://doi.org/10.1186/s40478-022-01331-w.

71. Ampofo, E., Sokolowsky, T., Götz, C., and Montenarh, M. (2013). Functional interaction of protein kinase CK2 and activating transcription factor 4 (ATF4), a key player in the cellular stress response. Biochim. Biophys. Acta *1833*, 439–451. https://doi.org/10.1016/j.bbamcr.2012.10.025.

72. Hughes, D.T., Halliday, M., Smith, H.L., Verity, N.C., Molloy, C., Radford, H., Butcher, A.J., and Mallucci, G.R. (2020). Targeting the kinase insert loop of PERK selectively modulates PERK signaling without systemic toxicity in mice. Sci. Signal. *13*, eabb4749. https://doi.org/10.1126/scisignal.abb4749.

73. Smith, H.L., and Mallucci, G.R. (2016). The unfolded protein response: mechanisms and therapy of neurodegeneration. Brain *139*, 2113–2121. https://doi.org/10.1093/brain/aww101.

74. Da Mesquita, S., Louveau, A., Vaccari, A., Smirnov, I., Cornelison, R.C., Kingsmore, K.M., Contarino, C., Onengut-Gumuscu, S., Farber, E., Raper, D., et al. (2018). Functional aspects of meningeal lymphatics in ageing and Alzheimer's disease. Nature *560*, 185–191. https://doi.org/10.1038/s41586-018-0368-8.

75. Wang, L., Zhang, Y., Zhao, Y., Marshall, C., Wu, T., and Xiao, M. (2019). Deep cervical lymph node ligation aggravates AD-like pathology of APP/PS1 mice. Brain Pathol. *29*, 176–192. https://doi.org/10.1111/bpa.12656.

76. Habib, N., McCabe, C., Medina, S., Varshavsky, M., Kitsberg, D., Dvir-Szternfeld, R., Green, G., Dionne, D., Nguyen, L., Marshall, J.L., et al. (2020). Disease-associated astrocytes in Alzheimer's disease and aging. Nat. Neurosci. *23*, 701–706. https://doi.org/10.1038/s41593-020-0624-8.

77. Liu, C.C., Hu, J., Zhao, N., Wang, J., Wang, N., Cirrito, J.R., Kanekiyo, T., Holtzman, D.M., and Bu, G. (2017). Astrocytic LRP1 Mediates Brain Abeta Clearance and Impacts Amyloid Deposition. J. Neurosci. *37*, 4023–4031. https://doi.org/10.1523/JNEUROSCI.3442-16.2017.

78. Wojtas, A.M., Sens, J.P., Kang, S.S., Baker, K.E., Berry, T.J., Kurti, A., Daughrity, L., Jansen-West, K.R., Dickson, D.W., Petrucelli, L., et al. (2020). Astrocyte-derived clusterin suppresses amyloid formation in vivo. Mol. Neurodegener. *15*, 71. https://doi.org/10.1186/s13024-020-00416-1.

79. Mahan, T.E., Wang, C., Bao, X., Choudhury, A., Ulrich, J.D., and Holtzman, D.M. (2022). Selective reduction of astrocyte apoE3 and apoE4 strongly reduces Abeta accumulation and plaque-related pathology in a mouse model of amyloidosis. Mol. Neurodegener. *17*, 13. https://doi.org/10.1186/s13024-022-00516-0.

80. Wang, C., Xiong, M., Gratuze, M., Bao, X., Shi, Y., Andhey, P.S., Manis, M., Schroeder, C., Yin, Z., Madore, C., et al. (2021). Selective removal of astrocytic APOE4 strongly protects against tau-mediated neurodegeneration and decreases synaptic phagocytosis by microglia. Neuron *109*, 1657–1674.e7. https://doi.org/10.1016/j.neuron.2021.03.024.

81. Sheehan, P.W., Nadarajah, C.J., Kanan, M.F., Patterson, J.N., Novotny, B., Lawrence, J.H., King, M.W., Brase, L., Inman, C.E., Yuede, C.M., et al. (2023). An astrocyte BMAL1-BAG3 axis protects against alpha-synuclein and tau pathology. Neuron *111*, 2383–2398.e7. https://doi.org/10.1016/j.neuron.2023.05.006.

82. Deng, Z., Jiang, J., Wang, J., Pan, D., Zhu, Y., Li, H., Zhang, X., Liu, X., Xu, Y., Li, Y., et al. (2022). Angiotensin Receptor Blockers Are Associated With a Lower Risk of Progression From Mild Cognitive Impairment to Dementia. Hypertension *79*, 2159–2169. https://doi.org/10.1161/HYPERTENSIONAHA.122.19378.

83. Shigetomi, E., Bushong, E.A., Haustein, M.D., Tong, X., Jackson-Weaver, O., Kracun, S., Xu, J., Sofroniew, M.V., Ellisman, M.H., and Khakh, B.S. (2013). Imaging calcium microdomains within entire astrocyte territories and endfeet with GCaMPs expressed using adeno-associated viruses. J. Gen. Physiol. *141*, 633–647. https://doi.org/10.1085/jgp.201210949.

84. Hao, Y., Stuart, T., Kowalski, M.H., Choudhary, S., Hoffman, P., Hartman, A., Srivastava, A., Molla, G., Madad, S., Fernandez-Granda, C., and Satija, R. (2024). Dictionary learning for integrative, multimodal and scalable single-cell analysis. Nat. Biotechnol. *42*, 293–304. https://doi.org/10.1038/s41587-023-01767-y.

85. Lee, Y.K., Uchida, H., Smith, H., Ito, A., and Sanchez, T. (2019). The isolation and molecular characterization of cerebral microvessels. Nat. Protoc. *14*, 3059–3081. https://doi.org/10.1038/s41596-019-0212-0.

86. Matthes, F., Matuskova, H., Arkelius, K., Ansar, S., Lundgaard, I., and Meissner, A. (2021). An Improved Method for Physical Separation of Cerebral Vasculature and Parenchyma Enables Detection of Blood-Brain-Barrier Dysfunction. Neurosci. *2*, 59–74. https://doi.org/10.3390/neurosci2010004.

87. Chen, K., Hu, Q., Xie, Z., and Yang, G. (2022). Monocyte NLRP3-IL-1beta Hyperactivation Mediates Neuronal and Synaptic Dysfunction in Perioperative Neurocognitive Disorder. Adv. Sci. (Weinh) *9*, e2104106. https://doi.org/10.1002/advs.202104106.

88. Schmidt, E.K., Clavarino, G., Ceppi, M., and Pierre, P. (2009). SUnSET, a nonradioactive method to monitor protein synthesis. Nat. Methods *6*, 275–277. https://doi.org/10.1038/nmeth.1314.

89. Yang, G., Pan, F., Parkhurst, C.N., Grutzendler, J., and Gan, W.B. (2010). Thinned-skull cranial window technique for long-term imaging of the cortex in live mice. Nat. Protoc. *5*, 201–208. https://doi.org/10.1038/nprot.2009.222.

90. Yang, G., Pan, F., Chang, P.C., Gooden, F., and Gan, W.B. (2013). Transcranial two-photon imaging of synaptic structures in the cortex of

awake head-restrained mice. Methods Mol. Biol. *1010*, 35–43. https://doi.org/10.1007/978-1-62703-411-1_3.

91. Xavier, A.L.R., Hauglund, N.L., von Holstein-Rathlou, S., Li, Q., Sanggaard, S., Lou, N., Lundgaard, I., and Nedergaard, M. (2018). Cannula Implantation into the Cisterna Magna of Rodents. J. Vis. Exp. *135*, 57378. https://doi.org/10.3791/57378.
92. Plá, V., Bork, P., Harnpramukkul, A., Olveda, G., Ladrón-de-Guevara, A., Giannetto, M.J., Hussain, R., Wang, W., Kelley, D.H., Hablitz, L.M., and Nedergaard, M. (2022). A real-time in vivo clearance assay for quantification of glymphatic efflux. Cell Rep. *40*, 111320. https://doi.org/10.1016/j.celrep.2022.111320.
93. Rustenhoven, J., Pavlou, G., Storck, S.E., Dykstra, T., Du, S., Wan, Z., Quintero, D., Scallan, J.P., Smirnov, I., Kamm, R.D., and Kipnis, J. (2023). Age-related alterations in meningeal immunity drive impaired CNS lymphatic drainage. J. Exp. Med. *220*, e20221929. https://doi.org/10.1084/jem.20221929.

Please cite this article in press as: Chen et al., Selective removal of astrocytic PERK protects against glymphatic impairment and decreases toxic aggregation of β-amyloid and tau, Neuron (2025), https://doi.org/10.1016/j.neuron.2025.04.027

STAR★METHODS

KEY RESOURCES TABLE

REAGENT or RESOURCE	SOURCE	IDENTIFIER
Antibodies		
Rabbit monoclonal anti-phospho-PERK (Thr980) (16F8)	Cell Signaling Technology	Cat#3179; RRID: AB_2095853
Rabbit monoclonal anti-PERK (D11A8)	Cell Signaling Technology	Cat#5683; RRID: AB_10841299
Mouse monoclonal anti-eIF2α (L57A5)	Cell Signaling Technology	Cat#2103; RRID: AB_836874
Rabbit monoclonal anti-phospho-eIF2α (Ser51) (D9G8)	Cell Signaling Technology	Cat#3398; RRID: AB_2096481
Rabbit monoclonal anti-β-Amyloid (D54D2)	Cell Signaling Technology	Cat#8243; RRID: AB_2797642
Mouse monoclonal anti-GFAP (GA5)	Cell Signaling Technology	Cat#3670; RRID: AB_561049
Rabbit monoclonal anti-β-Actin (13E5)	Cell Signaling Technology	Cat#4970; RRID: AB_2223172
Rabbit monoclonal anti-β-Tubulin (9F3)	Cell Signaling Technology	Cat#2128; RRID: AB_823664
Mouse monoclonal anti-GAPDH (D4C6R)	Cell Signaling Technology	Cat#97166; RRID: AB_2756824
Anti-rabbit IgG, HRP-linked	Cell Signaling Technology	Cat#7074; RRID: AB_2099233
Anti-mouse IgG, HRP-linked	Cell Signaling Technology	Cat#7076; RRID: AB_330924
Mouse monoclonal anti-phospho-Tau (Ser202, Thr205) (AT8)	Thermo Fisher Scientific	Cat#MN1020; RRID: AB_223647
Mouse monoclonal anti-phospho-Tau (Ser202, Thr205) (AT8), Biotin	Thermo Fisher Scientific	Cat#MN1020B; RRID: AB_223648
Rabbit polyclonal anti-GRP78	Thermo Fisher Scientific	Cat#PA1-014A; RRID: AB_559362
Rat monoclonal anti-CD68 (FA-11)	Thermo Fisher Scientific	Cat#14-0681-82; RRID: AB_2572857
Rat monoclonal anti-LYVE1 (ALY7), Alexa Fluor™ 488	Thermo Fisher Scientific	Cat#53-0443-82; RRID: AB_1633415
Donkey polyclonal anti-rabbit IgG, Alexa Fluor™ 488	Thermo Fisher Scientific	Cat#A-21206; RRID: AB_2535792
Donkey polyclonal anti-rabbit IgG, Alexa Fluor™ 647	Thermo Fisher Scientific	Cat#A-31573; RRID: AB_2536183
Donkey polyclonal anti-rat IgG, Alexa Fluor™ Plus 647	Thermo Fisher Scientific	Cat#A48272; RRID: AB_2893138
Donkey polyclonal anti-mouse IgG, Alexa Fluor™ 568	Thermo Fisher Scientific	Cat#A10037; RRID: AB_11180865
Goat polyclonal anti-mouse IgG, Alexa Fluor™ Plus 488	Thermo Fisher Scientific	Cat#A32723; RRID: AB_2633275
Chicken polyclonal anti-GFAP	Abcam	Cat#ab4674; RRID: AB_304558
Mouse monoclonal anti-CD31 (P2B1)	Abcam	Cat#ab24590; RRID: AB_448167
Mouse monoclonal anti-β-Amyloid 1–16 (6E10)	BioLegend	Cat#803001; RRID: AB_2564653
Rat monoclonal anti-mouse I-A/I-E, Alexa Fluor® 594	BioLegend	Cat#107650; RRID: AB_2566438
Rat monoclonal anti-mouse CD206, Alexa Fluor® 647	BioLegend	Cat#141712; RRID: AB_10900420
Rabbit polyclonal anti-phospho-PERK(Thr980)	Bioss	Cat#bs-3330R; RRID: AB_10855345
Guinea pig polyclonal anti-S100β	Synaptic Systems	Cat#287 004; RRID: AB_2620025
Rabbit polyclonal anti-aquaporin 4	Sigma-Aldrich	Cat#HPA014784; RRID: AB_1844967
Rabbit polyclonal anti-phospho-eIF2α (Ser51)	ImmunoWay	Cat#YP0093; RRID: AB_3065164
Mouse monoclonal anti-puromycin (12D10)	Sigma-Aldrich	Cat#MABE343; RRID: AB_2566826
Rabbit polyclonal anti-Iba1	Wako	Cat#019-19741; RRID: AB_839504
Mouse monoclonal anti-Tau (MC1)	Peter Davies, Albert Einstein College of Medicine	Cat#MC1; RRID: AB_2314773
Mouse monoclonal anti-casein kinase IIα (1AD9)	Santa Cruz Biotechnology	Cat#sc-12738; RRID: AB_2276843
Mouse monoclonal anti-human Casein Kinase 2 alpha (844720)	R&D	Cat#MAB7957; RRID: AB_3073948
Goat polyclonal anti-chicken IgG, Alexa Fluor™ 488	Molecular Probes	Cat#A-11039; RRID: AB_142924
Bacterial and virus strains		
AAV5-gfaABC1D-tdTomato	Shigetomi et al.[83]	Addgene 44332-AAV5

(*Continued on next page*)

Please cite this article in press as: Chen et al., Selective removal of astrocytic PERK protects against glymphatic impairment and decreases toxic aggregation of β-amyloid and tau, Neuron (2025), https://doi.org/10.1016/j.neuron.2025.04.027

Continued

REAGENT or RESOURCE	SOURCE	IDENTIFIER
Biological samples		
Human brain tissue	The New York Brain Bank	http://cumc.columbia.edu/dept/taub
Chemicals, peptides, and recombinant proteins		
Puromycin	Sigma-Aldrich	Cat#P8833
GSK2606414	Sigma-Aldrich	Cat#516535
Methoxy-X04	Sigma-Aldrich	Cat#SML3861
Thioflavin S	Sigma-Aldrich	Cat#T1892
Casein Kinase II	Sigma-Aldrich	Cat#218701
Dextran, Fluorescein, 3000 MW, Anionic	Thermo Fisher Scientific	Cat#D3305
Albumin from Bovine Serum (BSA), Alexa Fluor™ 647 conjugate	Thermo Fisher Scientific	Cat#A34785
CX-4945	MedChemExpress	Cat#HY-50855
TGN-020	Tocris	Cat#5425
Critical commercial assays		
Mouse TNF-α ELISA kit	Thermo Fisher Scientific	Cat#BMS607-3
Mouse IL-1β ELISA kit	Thermo Fisher Scientific	Cat#BMS6002
Mouse Aβ 40 ELISA kit	Thermo Fisher Scientific	Cat#KMB3481
Mouse Aβ 42 ELISA kit	Thermo Fisher Scientific	Cat#KMB3441
Human Tau (Total) ELISA kit	Thermo Fisher Scientific	Cat#KHB0041
Pierce™ BCA Protein Assay Kit	Thermo Fisher Scientific	Cat#23225
Mouse Anti-ACSA-2 MicroBead Kit	Miltenyi Biotec	Cat#130-097-678
Mouse Adult Brain Dissociation Kit	Miltenyi Biotec	Cat#130-107-677
RNAscope™ Multiplex Fluorescent Reagent Kit v2	Advanced Cell Diagnostics	Cat#323100
VECTASTAIN® Elite® ABC-HRP Kit, Peroxidase (Standard)	Vector Laboratories	Cat#PK-6100
Deposited data		
Mouse snRNA-seq	Zhou et al.[28]	GEO: GSE140511
Experimental models: Organisms/strains		
Mouse: C57BL/6J	The Jackson Laboratory	RRID: IMSR_JAX:000664
Mouse: $PERK^{loxP}$	The Jackson Laboratory	RRID: IMSR_JAX:023066
Mouse: Aldh1l1-Cre/ERT2	The Jackson Laboratory	RRID: IMSR_JAX:029655
Mouse: PS19	The Jackson Laboratory	RRID: IMSR_JAX:008169
Mouse: 5XFAD	The Jackson Laboratory	RRID: MMRRC_034840-JAX
Oligonucleotides		
RNAscope™ Probe-Mm-Eif2ak3-C1	Advanced Cell Diagnostics	Cat#1041101-C1
Software and algorithms		
Seurat v5	Hao et al.[84]	https://satijalab.org/seurat/

EXPERIMENTAL MODEL AND STUDY PARTICIPANT DETAILS

Animals

The transgenic mouse strains used in this study included 5XFAD (JAX #034840),[33] PS19 (JAX #008169),[39] $PERK^{flox}$ (JAX #023066),[30] and $Aldh1l1^{Cre/ERT2}$ (JAX #029655),[29] all obtained from The Jackson Laboratory. Mice were group-housed in temperature- and humidity-controlled rooms under a 12-h light/dark cycle and were randomly assigned to treatment groups. Both male and female mice were used in experiments. All animals were housed at the Columbia University animal facility and cared for in accordance with the National Institutes of Health (NIH) guidelines for the care and use of laboratory animals. All experimental procedures were approved by the Institutional Animal Care and Use Committee (IACUC) at Columbia University.

Human post-mortem brain tissue

Human brain specimens were obtained from the New York Brain Bank, with all diagnoses made by specialized neuropathologists. Study protocols were approved by the Institutional Review Board at Columbia University Medical Center. All clinical samples were de-identified prior to analysis, and all procedures were conducted in accordance with the ethical principles outlined in the World Medical Association Declaration of Helsinki and the Belmont Report issued by the U.S. Department of Health and Human services. Detailed subject information is provided in Table S1.

METHOD DETAILS

Analysis of snRNA-seq data

Single-nucleus RNA sequencing (snRNA-seq) data (GSE140511)[28] were analyzed using the *Seurat* package in R[84] (Figures 1A, 1B, S1, and S7A). Quality control procedures included the removal of nuclei with mitochondrial transcript content greater than 5% and the exclusion of potential doublets or multiplets based on unique molecular identifier (UMI) counts and gene numbers.[28] Principal component analysis (PCA) was performed, and the top 20 principal components were used for uniform manifold approximation and projection (UMAP). Clustering was conducted with a resolution of 0.1, and differential expression between clusters was assessed using the Wilcoxon rank-sum test.

RNA *in situ* hybridization

RNAscope *in situ* hybridization was used to detect *Eif2ak3* mRNA expression in astrocytes. Fresh-frozen brain slices (20 μm) were prepared, and a multiplex fluorescent assay was performed according to the manufacturer's instructions (Advanced Cell Diagnostics, ACD). Sections were incubated with a probe targeting *Eif2ak3* (1041101-C1, ACD) and labeled with a fluorescent dye (323100, ACD), followed by immunofluorescent staining for the astrocytic marker S100β (287 004, Synaptic Systems).

Immunofluorescence and immunohistochemistry

For immunofluorescent staining, coronal brain sections were washed twice with phosphate-buffered saline (PBS; AM9624, Thermo Fisher Scientific), permeabilized, and blocked for 2 h at room temperature in PBS containing 1% Triton X-100 (T9284, Sigma-Aldrich) and 1% serum (donkey, 017-000-121, or goat, 005-000-121; Jackson ImmunoResearch). Sections were then incubated overnight at 4°C with primary antibodies targeting: GFAP, phospho-PERK (Thr980), puromycin, AQP4, CD31, LYVE1, CD206, MHCII, Iba1, CD68, β-amyloid (D54D2 and 6E10), phospho-tau (AT8), pathological tau (MC1), or CK2α (mouse or human). Following primary antibody incubation, sections were washed and incubated with Alexa Fluor-conjugated secondary antibodies for 2 h at room temperature. After final PBS washes, sections were mounted using DAPI Fluoromount-G® (0100-20, SouthernBiotech) and imaged using confocal microscopy.

For core plaque assessment in 5XFAD mice, sections were dried overnight after immunostaining, rehydrated in Tris-buffered saline (TBS; J60764.K2, Thermo Fisher Scientific) for 30 s, and transferred to 40% ethanol in TBS for 30 s. Sections were incubated with 1 μM methoxy-X04 (SML3861, Sigma-Aldrich) in 40% ethanol for 3 min, followed by sequential rinses in 40% ethanol (30 s) and 95% ethanol (30 s), air-dried, and mounted for microscopy.

For diaminobenzidine (DAB) staining with a biotin-conjugated AT8 antibody, brain sections were washed with TBS and incubated for 20 min in a quenching solution (500 μL MeOH, 500 μL 30% H_2O_2, and 4 mL TBS). After two washes, sections were blocked and incubated overnight at 4°C with the biotin-conjugated AT8 antibody. Sections were then incubated with ABC-HRP reagent (PK-6100, Vector Laboratories) for 30 min, washed, and developed using DAB substrate (ab64238, Abcam) for 5–10 min before mounting in Fluoromount-G® (0100-01, Southern Biotech).

To visualize tau aggregates in PS19 mice, sections were stained with 1% thioflavin S (T1892, Sigma-Aldrich) in TBS for 8 min, followed by two rinses in 40% ethanol in TBS (2 min each), two PBS washes, and mounting on glass slides.

Confocal and widefield microscopy

To quantify *Eif2ak3* puncta and p-PERK expression in astrocytes, images of brain sections were acquired using a Zeiss 710 confocal microscope equipped with a 20× objective and 2.0× digital zoom. Z-stack images were collected with a 4 μm step size over a total depth of 40 μm. For *Eif2ak3* puncta analysis, 7–8 astrocytes per mouse were analyzed, totaling 36 cell somas across 5 mice. For p-PERK immunofluorescence analysis, 12 astrocytes per mouse were analyzed, totaling 72 cells across 6 mice. In human AD brain samples, 16 astrocytes per sample were analyzed, totaling 80 cells across 5 individuals.

To quantify D54D2, 6E10, AT8, and MC1 staining, fluorescent images were acquired using a Leica DMi8 widefield microscope with a 5× objective and 1.0× zoom, using a single focal plane. Identical laser intensities and exposure times were applied within each experimental cohort to ensure consistency. Fluorescent signal intensity and area coverage were quantified using uniform thresholding across all samples.

Isolation of astrocytes

Astrocytes were isolated using Magnetic-Activated Cell Sorting (MACS) following the manufacturer's protocol (130-097-678, Miltenyi Biotec). Briefly, mice were deeply anesthetized and transcardially perfused with PBS. After removal of the meninges, the cerebral

cortex was dissected and enzymatically dissociated using the Adult Brain Dissociation Kit (130-107-677, Miltenyi Biotec) in combination with the gentleMACS Dissociator (130-096-427, Miltenyi Biotec). The resulting cell suspension was collected by centrifugation (300 × g, 3 min) and filtered through a 70-μm strainer (130-098-462, Miltenyi Biotec). Cell pellets were washed, centrifuged, and resuspended in PBS.

The single-cell suspension was incubated at 4°C for 10 min with 15 μL of anti-myelin microbeads, gently mixed every 5 min. Myelin debris and mature oligodendrocytes were depleted using an LS column and MACS separator. The flow-through was centrifuged, resuspended in PBS, and incubated for 10 min at 4°C with 15 μL of Fc receptor blocking reagent (from the anti-ACSA-2 MicroBeads kit,130-097-678, Miltenyi Biotec), followed by a 10-min incubation with 15 μL of anti-ACSA-2 MicroBeads. After removing excess beads, astrocytes were enriched using an LC column and MACS separator. The astrocyte fraction was collected by removing the magnetic separator, centrifuging the pellets, and recovering the purified astrocytes. Isolated astrocyte pellets were snap-frozen in liquid nitrogen and stored at –80°C for subsequent immunoblotting.

Isolation of brain vessels

Brain vessels were isolated using previously described protocols.[85,86] Mice were deeply anesthetized and perfused with PBS. The brain was immediately collected on ice, and the cortex from one hemisphere was dissected. Cortical tissue was homogenized by repeated aspiration and expulsion through 21-gauge cannulas. The homogenate was centrifuged at 2000 × g for 10 min at 4°C, and the supernatant was discarded. The pellet was resuspended in 3 mL of ice-cold dextran solution in HBSS (14170112, Thermo Fisher Scientific), vigorously mixed for 1 min, and centrifuged at 4400 × g for 15 min at 4°C. After centrifugation, the top layer was carefully removed, and the vessel-enriched pellet was resuspended in HBSS containing 1% bovine serum albumin (BSA; A7030, Sigma-Aldrich). The resuspended vessels were filtered through a 20-μm mesh by centrifugation at 200 × g for 1 min and washed with HBSS. The final vessel fraction was collected and stored at –80°C for subsequent Western blot analysis.

Western blot

Proteins extracted from isolated astrocytes or brain vessels were thawed in 100 μL of radioimmunoprecipitation assay (RIPA) buffer (R0278, Sigma-Aldrich) supplemented with 10 mM Tris and protease and phosphatase inhibitors (78440, Thermo Fisher Scientific). Samples were homogenized using a glass micro-homogenizer (20–30 strokes) and incubated on ice for 30 min. Insoluble material was removed by centrifugation at 20,000 × g for 10 min at 4°C. Protein concentrations were determined using the BCA Protein Assay Kit (23225, Thermo Fisher Scientific).

Western blotting was performed as previously described.[87] Protein samples were mixed with 4× sample loading buffer, heated at 95°C for 10 min, separated on 10% or 12% SDS-PAGE gels, and transferred to PVDF membranes. Membranes were washed twice with TBS-Tween buffer and blocked with 1% BSA for 1 h at room temperature. Membranes were then incubated overnight at 4°C with primary antibodies targeting: BiP/GRP78, phospho-PERK (Thr980), PERK, phospho-eIF2α (Ser51), eIF2α, AQP4, β-actin, GAPDH, or β-tubulin. Following primary antibody incubation, membranes were washed four times with TBS-Tween (28360, Thermo Fisher Scientific) and incubated with the appropriate HRP-linked secondary antibody (anti-rabbit IgG or anti-mouse IgG).

Protein bands were visualized using the ImageQuant™ LAS 4000 biomolecular imager (GE Healthcare), and densitometric analysis was performed using NIH ImageJ software.

Measurement of *de novo* protein synthesis

De novo protein synthesis was assessed using the Surface Sensing of Translation (SUnSET) method,[88] which detects puromycin incorporation into nascent polypeptides as a marker of translation activity. The *in vivo* procedure was adapted from a previously published protocol.[32] To label astrocytes, 0.25 μL of AAV5-gfaABC1D-tdTomato (7×10^{12} genome copies/mL; 44332, Addgene)[83] was injected into the somatosensory cortex of 5-month-old WT and 5XFAD mice (coordinates: anterior-posterior (AP) +0.5 mm; midline (ML) +2 mm; depth 500 μm) using a picospritzer (5 p.s.i., 12 ms pulse width, 0.3–0.4 Hz) at a rate of 0.1 μL per 10–15 min. After injection, the micropipette was left in place for an additional 10–15 min to allow for viral diffusion before withdrawal. At 6 months of age, mice were implanted with an intracranial cannula targeting the same cortical region. Puromycin (5 μg; P8833, Sigma-Aldrich) was infused using an infusion pump connected to a Hamilton syringe. Following infusion, mice were returned to their home cage for 1 h to allow incorporation of puromycin into newly synthesized proteins. Brains were then collected and processed for immunofluorescent staining. For *in vitro* analysis, isolated astrocytes were incubated with 2 μM puromycin for 30 min at 37°C. After incubation, cells were lysed, and protein concentrations were normalized prior to Western blot analysis to assess puromycin incorporation.

AQP4 expression and polarization analysis

Perivascular AQP4 expression and polarization were quantified by analyzing AQP4 immunoreactivity in 10–15 $CD31^+$ vessel segments per mouse. The average value across segments was used to calculate expression and polarization levels for each animal. This approach was adapted from previously established protocols.[25,26,55] Perivascular AQP4 expression was quantified by measuring AQP4 fluorescence intensity specifically within the $CD31^+$ vascular regions. To assess AQP4 polarization, the median AQP4 fluorescence intensity within the perivascular regions was determined. Threshold analysis was then applied to calculate the percentage of the surrounding astrocytic area exhibiting AQP4 signal equal to or greater than the perivascular intensity. Polarization was defined as the percentage of the area with AQP4 immunoreactivity lower than that of the astrocytic endfeet in direct contact with the vasculature.

Please cite this article in press as: Chen et al., Selective removal of astrocytic PERK protects against glymphatic impairment and decreases toxic aggregation of β-amyloid and tau, Neuron (2025), https://doi.org/10.1016/j.neuron.2025.04.027

Thinned-skull cranial window

To preserve meningeal lymphatic drainage and cerebral arterial pulsation during *in vivo* imaging of fluorescent CSF tracers, a thinned-skull cranial window was prepared as previously described.[89,90] Mice were anesthetized with 100 mg/kg ketamine and 15 mg/kg xylazine. A custom head holder was secured to the skull using cyanoacrylate glue (Loctite 495) and dental cement (Metabond, Parkell), and the head was fixed onto a custom-built imaging plate. A circular region of the skull (2–3 mm in diameter) was marked at coordinates AP –0.5 mm and ML +1.5 mm. The skull surface was immersed in artificial cerebrospinal fluid (ACSF), and a high-speed micro drill was used to thin the marked area under a dissecting microscope. Drilling was performed intermittently to prevent overheating, with frequent replacement of ACSF to soften the bone and dissipate heat. Bone debris was continuously flushed away during the process. Once most of the spongy bone was removed, a microsurgical blade was used to carefully thin the remaining bone layer, creating a clear imaging window. The entire procedure was completed within 20 min. Throughout the surgery, the mouse's body temperature was continuously monitored and maintained at 37°C using a feedback-controlled heating system (World Precision Instruments).

Cisterna magna cannulation

Cisterna magna cannulation was performed to deliver CSF tracers immediately prior to *in vivo* imaging, as previously described.[12,91] Mice were anesthetized, and the posterior atlanto-occipital membrane overlying the cisterna magna was carefully exposed with precision. A 30-gauge needle attached to polyethylene tubing was gently inserted through the membrane. The cannula was secured in place using surgical glue and reinforced with dental cement. Throughout the procedure and during recovery, the animal's body temperature was continuously maintained at 37°C using a feedback-controlled heating system.

CSF tracers and drugs

Fluorescein isothiocyanate-dextran (FITC-dextran; D3305, Thermo Fisher Scientific) and Alexa Fluor 647-conjugated bovine serum albumin (BSA-647; A34785, Thermo Fisher Scientific) were prepared at a concentration of 0.5% in ACSF. These tracers were delivered into the subarachnoid CSF via cisterna magna cannulation for both *in vivo* and *ex vivo* analyses.[12]

To pharmacologically inhibit PERK (Figure 4A), the small-molecule PERK inhibitor GSK2606414 (516535, Sigma-Aldrich) was infused into the CSF through cisterna magna cannulation using an Alzet Osmotic Pump (model AP-2006, Braintree Scientific). A total volume of 150 μL GSK2606414 (30 mM in ACSF containing 0.5% hydroxypropylmethyl cellulose and 0.1% Tween-80) was loaded into the pump and delivered at a rate of 0.15 μL/h for 6 weeks. Control mice received an ACSF vehicle infusion.

To inhibit AQP4 function (Figure S4A), the selective AQP4 inhibitor TGN-020[40] (5425, Tocris) was dissolved in 20% sulfobutylether-β-cyclodextrin (SBE-β-CD) in saline and administered intraperitoneally at a dose of 100 mg/kg once every three days for 30 days. Control animals received equivalent volumes of the vehicle solution (20% SBE-β-CD in saline).

To increase CK2 activity (Figure 7D), 5XFAD mice with astrocytic PERK deletion received a single intracisternal injection of exogenous CK2 (10 μM in ACSF, 10 μL; 218701, Sigma-Aldrich) 7 days prior to immunohistochemical (IHC) analysis of AQP4 expression and polarization at 6 months of age. In a separate experiment (Figure S7B), astrocytic PERK-deleted 5XFAD mice received daily intracisternal injections of CK2 (10 μM, 10 μL) for 14 consecutive days prior to AQP4 analysis.

To inhibit CK2 activity (Figure 7F), 5XFAD mice were treated with the CK2 inhibitor CX-4945 (75 mg/kg in saline, i.p.) once daily starting at 5 months of age. IHC and other measurements were performed at 6 months.

Two-photon imaging of CSF tracer and analysis

In vivo imaging of CSF tracer influx was performed using a Scientifica two-photon microscope equipped with a Ti:Sapphire laser (Vision S, Coherent). Mice with previously prepared thinned-skull windows and cisterna magna cannulation were anesthetized with ketamine and xylazine, and their heads were stabilized under the microscope.

Immediately before imaging, 10 μL of FITC-dextran was infused into the cisterna magna at a rate of 2 μL/min using a syringe pump. To visualize the vasculature, 0.1 mL of Texas Red-dextran 70 kDa was injected retro-orbitally. The laser was tuned to 920 nm to enable simultaneous excitation of FITC and Texas Red fluorophores. Images were captured using a 20× water-immersion objective (1.0 N.A.) with a digital zoom of 1.0 at a resolution of 512×512 pixels. Time-lapse z-stack images were acquired every 5 min, spanning from the cortical surface to a depth of 250 μm with a 4 μm step size. Image acquisition was controlled using ScanImage software (v5.4; Vidrio Technologies).

Imaging data were analyzed using NIH ImageJ software.[12,52,55] Optical sections at a depth of 100 μm below the cortical surface were selected for quantification of CSF tracer penetration kinetics. Penetrating arterioles were distinguished from venules based on morphological characteristics, including fewer branches and superficial cortical positioning. To measure CSF–ISF exchange, donut-shaped regions of interest (ROIs) were defined around penetrating arterioles with an external diameter of 150 pixels and an internal diameter of 50 pixels. The mean fluorescence intensity within each ROI was calculated at each time point. Perivascular ROI values were averaged per animal per time point to generate a single biological replicate. Tracer dynamics were analyzed using two-way ANOVA followed by Bonferroni's *post hoc* test for multiple comparisons.

Ex vivo imaging of CSF tracer and analysis

For *ex vivo* assessment of CSF tracer influx, 10 μL of BSA-647 was injected into the cisterna magna, and brain tissue was collected 30 min later to evaluate tracer penetration into the parenchyma. Mean fluorescence intensity of BSA-647 in the somatosensory cortex

was quantified as previously described.[20] For each mouse, 3–5 coronal sections spanning –1.0 to +1.0 mm from bregma were selected, and tracer penetration was measured and averaged to generate a single biological replicate.

To assess CSF tracer drainage, 10 μL of BSA-647 was similarly injected into the cisterna magna, and the presence of tracer in the deep cervical lymph nodes (dCLNs) was evaluated 1 h post-injection. Quantification of BSA-647 signal in the dCLNs was performed as previously described.[92,93] For each animal, five 30-μm-thick dCLN sections were analyzed, and tracer fluorescence was measured and averaged for statistical analysis.

ELISA

Enzyme-linked immunosorbent assay (ELISA) was used to quantify concentrations of mouse $A\beta_{40}$ (KMB3481, Thermo Fisher Scientific), mouse $A\beta_{42}$ (KMB3441, Thermo Fisher Scientific), total human tau (KHB0041, Thermo Fisher Scientific), mouse IL-1β (BMS6002, Thermo Fisher Scientific), and mouse TNF-α (BMS6073, Thermo Fisher Scientific) in brain tissue samples.

For Aβ measurements in 5XFAD mice, the cortex and hippocampus were dissected following PBS perfusion, snap-frozen on dry ice, and stored at –80°C until processing. Soluble and insoluble fractions were extracted separately. Tissues were first sonicated in TBS and centrifuged at 15,000 × g for 15 min at 4°C. The resulting supernatant was collected as the soluble fraction. The pellet was resuspended in TBS containing 1% Triton X-100 (TBSX), incubated on ice for 1 h, and centrifuged again at 15,000 × g for 15 min at 4°C to obtain the detergent-soluble (TBSX) fraction. For extraction of the insoluble fraction, the remaining pellet was incubated in 5 M guanidine hydrochloride (GDN; G3272, Sigma-Aldrich), then centrifuged, and the supernatant was collected. $A\beta_{40}$ and $A\beta_{42}$ levels in all fractions were measured using the respective ELISA kits, according to the manufacturer's instructions.

For total human tau measurements in PS19 mice, cortical tissue was sonicated in reassembly (RAB) buffer (100 mM MES, 1 mM EGTA, 0.5 mM $MgSO_4$, 0.75 M NaCl, 20 mM NaF, supplemented with protease and phosphatase inhibitors), and centrifuged at 15,000 × g for 20 min at 4°C. The supernatant was collected as the RAB-soluble fraction. The pellet was resuspended in an equal volume of RIPA buffer and centrifuged to obtain the detergent-soluble (RIPA) fraction. The remaining pellet was then extracted with formic acid, and the supernatant collected as the insoluble fraction. Tau levels in all fractions were quantified using ELISA kits according to the manufacturer's protocols.

Behavior

Barnes maze

The Barnes maze test was used to assess spatial memory in mice.[36] The apparatus consisted of a circular platform (90 cm in diameter) with 19 evenly spaced holes along the perimeter, one of which served as the escape hole. An escape box (24 × 5 × 5 cm) was placed beneath this target hole to provide a refuge. Visual cues were positioned around the platform to facilitate navigation, and an auditory cue (buzzer) was used to motivate exploration. During the training phase, mice underwent one session per day for four consecutive days. At the start of each session, mice were placed in the center of the platform for a 5–10 s acclimation period, after which they were given 5 min to locate the escape cage. If a mouse failed to find the escape within the allotted time, it was gently guided to the target location. To minimize olfactory cues, the platform and escape box were cleaned with 75% alcohol between trials. A probe trial was conducted on the day following the final training session to assess spatial memory retention. During the probe trial, the escape box was removed, and mice were allowed to explore the platform for 3 min. Spatial memory was quantified as the percentage of time spent in the target quadrant where the escape hole had previously been located. Behavioral data were recorded and analyzed using ANY-maze software (Stoelting).

Auditory-cued fear conditioning

Auditory-cued fear conditioning was conducted in a dedicated conditioning chamber (Maze Engineers), with behavior data recorded and analyzed using ANY-maze software. The procedure began with a 2-min habituation period to allow mice to acclimate to the environment. The conditioning phase consisted of three cycles. Each cycle included a 30-s auditory cue (400 Hz, 80 dB) that co-terminated with a 2-s foot shock (0.5 mA), followed by a 30-s intertrial interval. Two minutes after the final conditioning cycle, mice were returned to their home cages. Memory recall tests were performed either 1 day or 7 days after conditioning. During recall, mice were placed in a novel chamber for a 2-min baseline period, followed by re-exposure to the same auditory cue. Freezing behavior, defined as the absence of all movement except respiration, was measured and analyzed using ANY-maze software.

QUANTIFICATION AND STATISTIAL ANALYSIS

Statistical analyses were performed using Prism 10 (GraphPad). Data are presented as mean ± SEM. Sample sizes for *in vivo* imaging, biochemical, and behavioral experiments were consistent with those reported in previous studies[36] and were not predetermined by power analysis. No successfully imaged or measured samples or animals were excluded from the analysis. The normality of data distribution was assessed using the Shapiro–Wilk test. Depending on the distribution, comparisons between two groups were made using either an unpaired two-tailed *t*-test (parametric) or the Wilcoxon rank-sum test (nonparametric). For comparisons involving more than two groups, one-way or two-way ANOVA was used, followed by Bonferroni's *post hoc* test for multiple comparisons. All statistical tests were two-sided, and significance was defined as $P \leq 0.05$.